‘Knock on nanocellulose’: Approaching the laminar burning velocity of powder-air flames

Audrey Santandrea, Marine Gavard, Stéphanie Pacault, Alexis Vignes, Laurent Perrin, Olivier Dufaud

'Knock on nanocellulose': approaching the laminar burning velocity of powder-air flames

Audrey Santandrea [1,2], Marine Gavard [1], Stéphanie Pacault [1], Alexis Vignes [2], Laurent Perrin [1], Olivier Dufaud [1,*]

***Corresponding author:** Olivier Dufaud (E-mail address: olivier.dufaud@univ-lorraine.fr)

[1] Laboratoire Réactions et Génie des Procédés, Université de Lorraine, CNRS, LRGP, F-54000 Nancy, France

[2] INERIS, Accidental Risks Division, Parc Technologique ALATA, BP 2, F-60550, Verneuil-en-Halatte, France

Abstract:

Due to their low sedimentation rate, nano-objects offer the opportunity to study flame propagation at low turbulence. The burning velocity was then estimated by flame visualization in two apparatuses: a vertical 1 meter long tube with a square cross-section and a 20L sphere equipped with visualization windows and a vent. This works aims to study the laminar burning velocity of nanocellulose by a direct visualization of the flame propagation within these devices. A high-speed video camera was used to record the flame propagation, and an estimation of the unstretched burning velocity was obtained through linear and nonlinear relationships relating the flame stretching and the flame velocities. Although these methods were initially established for gases, the organic nature of nanocellulose implies a fast devolatilization, which makes the application of the methods possible in this work. Similar results were obtained in both apparatuses in different turbulence conditions, proving the

laminar burning velocity was approached. The laminar burning velocity for the nanocellulose was determined to be 21 $cm.s^{-1}$. This value, estimated through flame propagation visualization, was then compared to the value calculated by applying a semi-empiric correlation to the pressure-time evolution recorded during standard explosion tests in the 20L vessel.

Keywords: Dust Explosion; Nanocellulose; Flame propagation; Burning Velocity; Nanopowder

1. Introduction

In order to assess explosion risks, the determination of key safety parameters is required (Eckhoff, 2003; Jespen, 2016). Among these parameters, the maximum explosion overpressure and the maximum rate of pressure rise are commonly used to characterize the explosion severity. Their determination implies controlled explosion tests in a closed vessel to measure the pressure evolution with time, which induces a volume-dependence of the results. To be able to design protection equipment, normalized test conditions and apparatuses are then needed. For instance, the EN 14034 standard is generally used, recommending tests in a 20L sphere or a $1m^3$ vessel under specific conditions (injection procedure, type of nozzle, ignition delay time, ignition source and energy, initial temperature and pressure).

However, standard conditions can be different from industrial conditions (Tamanini, 1990) and do not consider the specificities of each powder. For instance, the ignition energy is set at 10 kJ while the minimum ignition energy can be much lower, which can lead to an overdriving phenomenon and a misestimation of the risk (Going et al., 2000; Zhen and

Leuckel, 1997). Moreover, to represent the volume-dependence of the experimental explosion parameters, a 'cube-root law' was proposed by Bartknecht (1989) and demonstrated later by Eckhoff (2003). This law is valid under several assumptions considering that the vessels have similar geometries, the flame thickness is negligible with respect to the vessel radius, the burning velocity is the same in both volumes and point ignition occurs at the center of the vessels (Lewis and von Elbe, 1987; Skjold, 2003). Several tests have been performed to compare results obtained in the 20L sphere and the $1m^3$ vessel, revealing significant differences between the two vessels, thus questioning the validity of the cube-root law (Clouthier et al., 2019; Proust et al., 2007; van der Wel et al., 1992). It has notably been proven that radiation can play a significant role in dust combustion, which tends to increase the flame thickness and even invalidate the cube-root law in some cases, especially for metal particles (Bidabadi and Azad, 2015; Dahoe et al., 1996; Taveau et al., 2018). Discrepancies have also been found in terms of turbulence, showing the ignition delay time in both vessels does not allow the same initial turbulence of the dust cloud (Amyotte et al., 1988; Dahoe et al., 2001; Pu et al., 1991; van der Wel, 1993).

If the procedures to determine explosion safety parameters are relatively well defined for micro-powders, they are still subject to debate, especially for nanopowders. Several authors have highlighted, that due to their small size, nanoparticles develop a high specific surface area leading to specific explosion properties (Amyotte, 2014; Boilard et al., 2013; Bouillard et al., 2010; Eckhoff, 2012; Mittal, 2014; Vignes et al., 2019; Wu et al., 2014). Among these specificities, their high specific surface area can both lead to changes in the rate-limiting step of the oxidation reaction (Bouillard et al., 2010; Vignes et al., 2019) and to the modification of the dust cloud particle size distribution due to the agglomeration phenomenon (Eckhoff, 2012; Santandrea et al., 2019a). Moreover, other specificities may call into question the relevance of standardized tests in a closed vessel. For instance, due to their increased ignition

sensitivity, underlined notably by Krietsch et al. (2015), Mohan et al. (2012) and Sundaram et al. (2013), an overdriving or pre-ignition phenomenon is more likely to occur when testing nanopowders. Furthermore, the radiative heat transfer occurring during the flame propagation can be greatly affected by the agglomeration level of the dust cloud (Dufaud et al., 2011; Kosinski et al., 2013; Vignes, 2008). In the case of enhancement of the radiative transfer, the flame thickness would no longer be negligible with respect to the vessel radius, as assumed by the cube-root law. As a consequence, a direct transposition of the safety parameters from lab-scale to industrial-scale may be inaccurate.

To overcome the cube-root law limitations, flame propagation is often studied and used in Computational Fluid Dynamics (CFD) simulations to characterize gas explosion (Di Benedetto et al., 2013; Ghaffari et al., 2019; Skjold, 2003). The essential parameters are then the flame thickness and, more importantly, the laminar burning velocity (Belerrajoul, 2019; Dahoe et al., 2002a). This latter is a fundamental property of the fuel and only depends on the fuel nature and the mixture concentration (Miao et al., 2014). It can be used in simulations to evaluate the consequences of an explosion scenario with controlled conditions (Skjold, 2007; Tolias and Venetsanos, 2018). Although the estimation of the laminar burning velocity of gases is not trivial, the experimental determination of the laminar burning velocity of dust-air mixtures is much more difficult to perform than for gases due to the inherent turbulence related to the powder dispersion. Nevertheless, some experiments have been performed by various authors in a micro-gravity environment during a parabolic flight or using a drop tower (Goroshin et al., 2011; Lee et al., 1993; Pu et al., 1998; Tang et al., 2009). However, such tests being very expensive and difficult to perform on a large scale and with a high frequency, three more accessible methods for the determination of the unstretched burning velocity can be found in the literature: the burner method, with various existing configurations (Dahoe et al., 2002; Julien et al., 2017; Lomba et al., 2019; van der Wel, 1993), the contained explosions

method (Silvestrini et al., 2008; Skjold, 2003; van der Wel, 1993) and the tube method (Andrews and Bradley, 1972; Di Benedetto et al., 2011; Proust, 2006). However, test results obtained in turbulent conditions had to be numerically extrapolated to a zero degree of turbulence (Bradley et al., 1989); as a consequence, the term 'unstretched burning velocity' will be preferred to 'laminar flame velocity' to qualify the parameter obtained.

Despite the greater accessibility of these methods, experimental issues remain and usually limit the reproducibility and accuracy of the results. In addition to the stochastic nature of turbulence, issues can also come from particle agglomeration, instabilities of the biphasic flow, set-up fouling or flame front visualization difficulties. However, for specific reactive mixtures such inconveniences may be limited: for instance, testing gas-dust mixtures with a low dust concentration (called gas-driven hybrid mixtures) in a semi-open tube allowed the determination of their unstretched flame velocity and highlighted the influence of turbulence/combustion interactions on the flame propagation (Cuervo, 2015; Torrado et al., 2017b).

Similarly, the low inertia of nanoparticles allows tests with a long ignition delay time. Consequently, experiments can be performed at low turbulence with nanoparticles while sedimentation would occur for micropowders under the same experimental conditions. Decreasing the turbulence level of the initial dust cloud can help approaching the 'laminar flame velocity' of dust-air mixtures through the assessment of an unstretched flame velocity, which is then expected to be independent from turbulence. This concept will be developed through the characterization of the unstretched burning velocity of a nanocellulose powder using three different procedures and set-ups: a semi-opened tube, a vented vessel and the classical 20L explosion sphere.

2. Materials and methods

2.1. Nanocellulose characterization

In this study, an organic powder was chosen with regard to experimental, scientific and industrial considerations. First of all, the powder should display a sufficient ignition sensitivity to be ignited by an electrical spark and thus ensure a single point ignition, which is not the case of carbonaceous powders (Turkevich et al., 2016; Vignes, 2008). Moreover, metal nanopowders may be subjected to pre-ignition and their flame tend to propagate with a significant thermal radiation, which can hinder the flame front observation. Organic nanopowders, with a minimum ignition energy of a few millijoules and a flame propagation with limited thermal radiation, then appears to be a good solution. Moreover, during their combustion, the devolatilization step occurs rapidly, which can lead to flame propagation rather similar to those already observed for gas-powder hybrid mixtures (Cuervo, 2015) or flame propagation occurring in the gas phase (Bradley and Lee, 1984) and makes possible the application of relations initially established for such mixtures.

From an industrial point of view, nanocellulose is of increasing interest due to its specific chemical and physical properties providing a wide variety of applications, notably in photonics, medical devices, coating, electronics, 3D printing and plastics (Abitbol et al., 2016). The powder used in this study is a cellulose nanocrystals powder (NCC from CelluForce) with primary fiber dimensions of 3 nm width, an average length of 70 nm and a specific surface area of 400 $m^2.g^{-1}$, as specified by the producer (CelluForce, 2016). Although this powder is constituted of nanofibers, the word “nanoparticles” will be employed in this work with no distinction between fibers and particles. The nanocellulose was dried at 90°C under vacuum before performing tests to limit the influence of humidity on the explosion parameters and improve reproducibility. Nanocellulose was observed by Scanning Electron Microscopy (Figure 1) but did not reveal clearly the nanometric structure of the powder.

Additional experiments were performed with a rotative drum combined with a Condensation Particle Counter (CPC – TSI 3007) and demonstrate the presence of two modes at 2 µm and 20 nm. Further tests were performed directly after powder dispersion in the explosion vessels in order to highlight the presence of primary nanopowders in addition to the inevitable agglomerates.

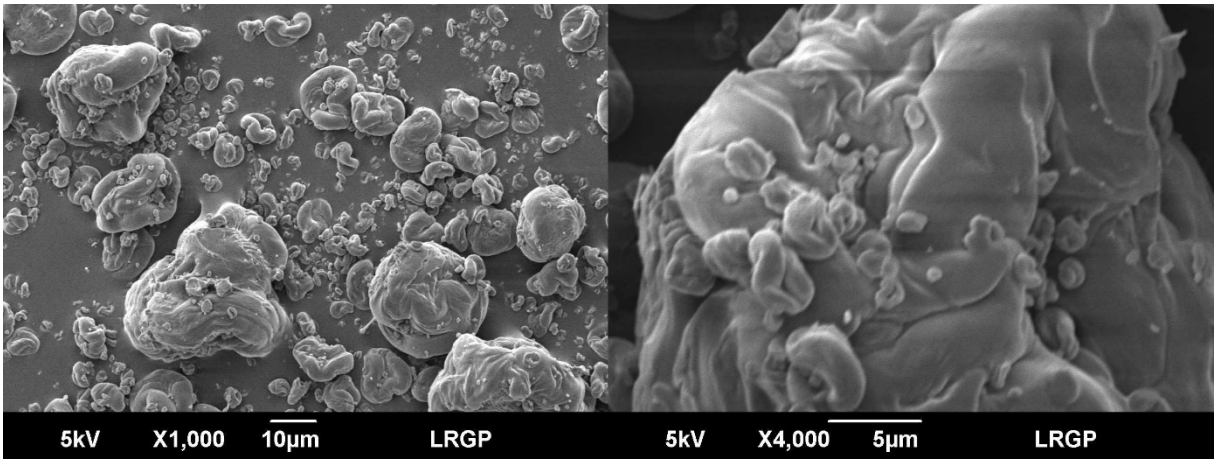

Figure 1 Nanocellulose observed with an Scanning Electron Microscope

2.2. Explosion tests equipment

The unstretched burning velocity of nanocellulose was estimated using three experimental methods. First, a flame propagation tube of 7 x 7 x 100 cm^3 open at its upper end and implementing the ignition system of the modified Hartmann tube, was coupled with a high-speed video camera at 4000 fps with 240 µs of exposure time (Phantom V9.1). Electrodes are located at 12.5 cm from the bottom of the tube. The equipment and procedure are fully described by Cuervo et al. (2017) and Torrado et al. (2017) who validated the set-up and procedure with methane and obtained encouraging results for hybrid mixtures. However, the small volume, especially around the ignition zone, implies that the flame is influenced by the walls quite soon after the ignition, which impacts its propagation. Therefore, the analysis is limited to the first moments of the flame kernel growth, between ignition and the flame spatial

164 acceleration (or quenching) due to the presence of the wall. Consequently, a second method
165 was developed to study flame propagation within a modified 20L sphere.

166 The standard apparatus described by European standards (EN 14034-1, 2004; EN 14034-2,
167 2006) does not allow a clear visualization of the content of the sphere, preventing the
168 observation of both the dust cloud after dispersion and the flame propagation. To overcome
169 this limitation, Murillo (2016) designed a new 20L sphere equipped with four visualization
170 windows made of borosilicate with a diameter of 9.7 cm on the lateral sides and one on the
171 top to characterize the dust cloud in terms of particle size distribution and turbulence. Torrado
172 (2017) adapted the apparatus to perform hybrid mixtures explosion tests and to study the
173 flame propagation. Therefore, a lateral window was removed to integrate an ignition source
174 composed of two tungsten electrodes connected to a KSEP 320 system (Kühner AG - 15 kV /
175 15 mA, i.e. 225 W) generating a permanent spark whose duration, and thus energy, can be
176 varied. A modification of the Kühner software was necessary to control accurately the
177 ignition delay time, called ‘tv’, when using the permanent spark. A pressure relief valve,
178 opening at 1.15 atm (abs), was added on top of the sphere to protect the windows during the
179 explosion. The flame front and shape are imaged using a Schlieren system, combined with the
180 high-speed camera. The Schlieren setup consists of a 150 W xenon lamp (66475-150XV-R22
181 Xenon Light Source) equipped with a lens, a pinhole with a diameter of 1 mm to obtain a
182 single-point light source, and a spherical mirror reflecting the punctual light toward a filter
183 placed in front of the camera (Figure 2). This technique, notably described by Mazumdar
184 (2013), allows the observation of density variations, which provides a better visualization of
185 the flame front.

186 The results obtained with both apparatuses were then compared to the correlations established
187 by Silvestrini et al. (2008), based on the evolution of the maximum overpressure and the
188 maximum rate of pressure rise during an explosion carried out in a closed vessel. To ensure a

proper comparison, explosions tests were performed in the standard 20L sphere with a permanent spark to avoid an overdriving phenomenon and a source ignition dependence of the results. Tests were also performed on nanocellulose according to the standard procedure (EN 14034-1:2004 + A1:2011; EN 14034-2: 2006 + A11:2011) and 10 kJ chemical igniters. The tube tests were performed at 300 mJ and in the 20L sphere, open and closed, an energy of 10J was used, knowing the minimum ignition energy of the chosen dried nanocellulose for those experiments is about 5 mJ as measured in a Mike 3 apparatus.

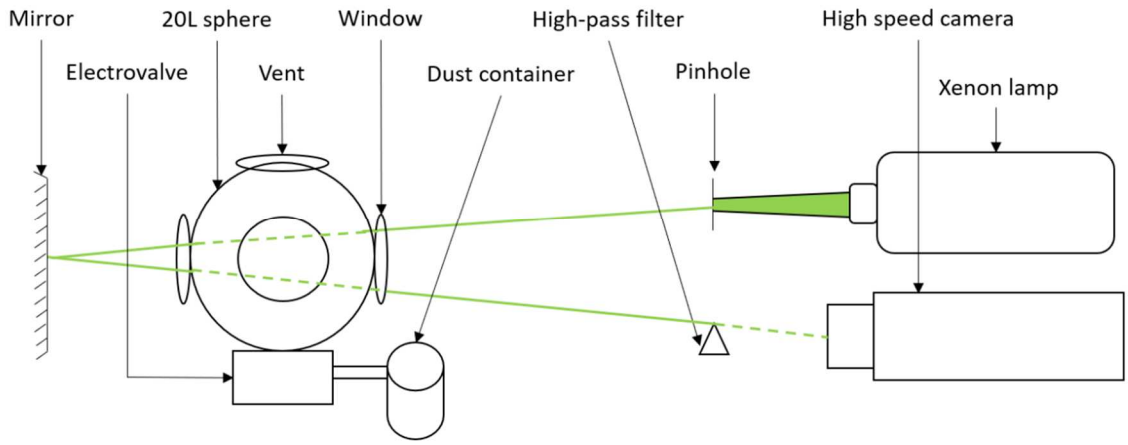

Figure 2. Schematic of the Schlieren setup and the modified 20L sphere

2.3. Dust cloud characterization

The particle size distribution of a dust cloud constituted of nanoparticles is one of the most important factors influencing the flame propagation but also one of the most complex to consider. Indeed, no apparatus or technique currently allows the determination at high frequency and high concentration, i.e. a concentration equal or greater than the usual minimum explosive concentrations (125 $g.m^{-3}$ for the chosen nanocellulose), over a whole range of particles sizes from 10 nm up to 200 µm.

206 To characterize the dust cloud, a laser diffraction sensor (Sympatec) was used through the
207 visualization window of the 20L sphere and the tube to measure the in-situ particle size
208 distribution (PSD) for particle sizes from 0.5 to 175 µm (R3 lens) at a frequency of 2 analyses
209 per millisecond. Since the combustion reaction can occur at the surface of the particles, as a
210 function of the reaction regime considered, the surface fraction is considered instead of the
211 usual volume fraction for the particle size distribution. It should be noted that other metrics,
212 such as the volume or number can also be considered to represent the particle size distribution
213 (Santandrea et al., 2019b).

214 In addition, the turbulence level of the dust cloud estimated by Dahoe et al. (2001) using a
215 laser Doppler anemometer was considered in the 20L sphere, and the measurements
216 performed by Particle Image Velocimetry (PIV) by Cuervo (2015) were used to estimate a
217 root-mean square velocity u_{rms} of the dust cloud in the flame propagation tube. Regarding the
218 values presented in Table 1, it appears that the turbulence level is always higher in the 20L
219 sphere than in the propagation tube, which is due to the high pressure applied during the
220 injection in the sphere and to the use of a dust canister. However, for both equipment, the
221 turbulence level decreases rapidly in the low ignition delay time range (from 60 to 120 ms,
222 71% lower in the 20L sphere and 39% in the tube) and seems to stabilize for high ignition
223 delay times (<200 ms), as discussed by Murillo et al. (2018) and Santandrea et al. (2019a).
224 Indeed, between 100 ms and 200 ms, the root-mean square velocity decreases 67% in the 20L
225 sphere and 60% in the tube, and only 14% in the 20L sphere and 25% in the tube between 300
226 ms and 400 ms. This "stable stage" allows to reach pseudo-laminar conditions and to
227 approach a laminar burning velocity when increasing sufficiently the ignition delay time.

228 *Table 1. Root mean square velocities measured in the 20L sphere and in the propagation tube*
229 *(Cuervo, 2015; Dahoe et al., 2001)*

230

Ignition delay time (ms)	u_{rms} in the 20L sphere ($m.s^{-1}$) (Dahoe et al., 2001)	u_{rms} in the propagation tube ($m.s^{-1}$) (Cuervo, 2015)
60	3.5	1.4
100	1.5	1.0
200	0.5	0.4
300	0.35	0.2
400	0.3	0.15

231

232 Explosion tests in the standard closed 20L sphere were performed according to EN 14034-
233 1:2004 + A1:2011 and EN 14034-2:2006 + A11:2011 on the nanocellulose and on
234 microcrystalline cellulose (Avicel, d_{50} = 108 µm) for comparison.

235 2.4. Assessment of unstretched flame velocity for nanopowders

236 The determination of the unstretched flame velocity was performed both by direct
237 visualization of the flame propagation and by analyzing the pressure-time curves recorded
238 during an explosion in the 20 L sphere.

239 2.4.1. Flame propagation experiments

240 2.4.1.1. Flame propagation and stretching observation

241 The propagation speed can be estimated using existing mathematical models based on several
242 hypotheses (Chen and Ju, 2007; Frankel and Sivashinsky, 1984; Joulin and Clavin, 1979).
243 The flame is then assumed to be spherically expanding and governed by an overall one-step
244 exothermic reaction, and the thermodynamic properties of the mixture such as the molecular
245 weight, the specific heat and the thermal conductivity are considered constant. The potential
246 heat losses are neglected and the combustion process is assumed to be isobaric, which seems
247 reasonable before the flame is affected by the vessel walls. With all these hypotheses, the
248 laminar burning velocity can be estimated using a linear or a non-linear methodology, from
249 the knowledge of the turbulent burning velocity and flame stretching.

To evaluate those parameters, flame propagation videos were analyzed by a model developed by Cuervo (2015) in MatLab's Simulink using the Vision toolbox (Cuervo et al., 2017; Torrado et al., 2017). This model isolates the flame profile for each frame of the video as shown in Figure 3 and calculates the position of the flame front z, the estimated cross-section area A_S and the estimated flame surface A_f. In the case of flame kernels growing spherically, the flame radius is generally considered to estimate the spatial velocity (Law, 2006; Varea, 2013). However, since the flame kernel appears to grow as an ellipsoid at low turbulence levels, the spatial velocity is calculated by deriving the position of the front flame.

Since the laminar flame velocity is independent of the vessel geometry and size, only the phase of 'free' flame kernel propagation is considered, i.e. when the flame is not significantly affected by the vessel walls, by compression or gas-wall heat transfers. It should be noted that, due to the contribution of the ignition source and the small size of the initial flame kernel, which can be located –with respect to the camera- behind unburnt particles, the very first milliseconds of the videos are also often delicate to analyze. The position of the flame z being known for different times, the spatial velocity of the flame S_S can be deduced. Then, the flame burning velocity S_u can be calculated using Andrews and Bradley (1972) formula:

$$S_u = S_s \frac{A_s}{A_f} \quad (1)$$

Figure 3. Time evolution of the flame profile in the semi-open tube for a dispersion of 500 g.m^{-3} of nanocellulose at 340 ms ignition delay time

This model is valid if the flame burning velocity S_u remains constant (which essentially means that the local fuel equivalence ratio does not change during the flame propagation), if the flame thickness is small in comparison to the flame curvature and if the spatial velocity S_S is uniform over the whole surface of the flame. However, in the context of these experiments, the ignition is performed 12.5 cm above the closed side of the tube, implying the hot burnt gases are pushing up the fresh gases due to their thermal expansion. Therefore, a thermal expansion factor χ, represented by the ratio between the temperatures of the hot burnt gases and the initial cold gases, should be introduced to correct this increased velocity. The temperature of the gases generated by the combustion reaction is approximated to be the adiabatic temperature at equilibrium conditions and is determined by the CEA software (McBride and Gordon, 1996). Equation (1) then becomes:

$$S_u = \frac{S_S}{\chi}\frac{A_S}{A_f} \tag{2}$$

However, as previously explained, only the "free" flame kernel propagation is considered, meaning the analysis is stopped when the flame is close to the walls but is still unaffected by their presence. This induces that, at this early stage, the flame kernel growth is unaffected by the thrust of the gases against the bottom of the tube and by the pressure increase taken into account by the thermal expansion factor.

It should be underlined that the burning velocity of a fuel-air mixture depends on the initial dust concentration, the pressure and the temperature, but also the turbulence. More than any other parameter, this point is very important and specific to dust explosions due to the inherent turbulence developed when generating the dust cloud. This effect can be estimated using the flame's stretching factor K, called Karlovitz factor (Karlovitz et al., 1951), defined as:

$$K = \frac{1}{A_f}\frac{dA_f}{dt} \quad (3)$$

The sign of the Karlovitz factor indicates the expansion (K positive) or compression (K negative) of the flame surface area. Since the stretching can be due to the curvature of the flame or to the strain rate of the flow, the stretching factor can be decoupled in two different variables K_c and K_s (Bradley, 2000). However, in this work, the flame stretching will be considered as a single phenomenon combining both effects.

In the literature, two relations to link the Karlovitz factor to the burning velocity are mainly used by considering the assumptions previously mentioned: a linear relation and a non-linear one. Although those relations were initially established for gases, Cuervo et al. (2017) and Torrado et al. (2017) obtained encouraging results by applying them to starch/methane as well as carbon nanoparticles/methane hybrid mixtures. In this work, the same relations are applied to pure dust explosions. Indeed, the low inertia of nanocellulose particles allows the measurement at very low turbulence, leading to a spherical/ellipsoidal flame kernel growth. Moreover, the organic nature of the chosen powder induces a fast devolatilization which implies that, under certain concentration and turbulence conditions, the dust combustion would be controlled by gas combustion (Di Benedetto and Russo, 2007).

2.4.1.2. Linear relation

Most of the authors studying flame propagation and laminar burning velocity (Cuervo et al., 2017; Dahoe et al., 2002; Di Benedetto et al., 2011) use a linear relation established for pure gases and stating that, in a first approach, the Karlovitz factor can be linked to the flame burning velocity by the following relationship (Clavin, 1985; Markstein, 1964):

$$S_u = -\delta_M K + {S_u}^0 \quad (4)$$

where $S_u°$ is the unstretched burning velocity and δ_M, the Markstein length, whose sign provides an indication on the stability of the flame (Clavin, 1985). This linear relation is valid if the flame stretching is weak, i.e. if the Karlovitz number is low, and if the ratio of thermal diffusivity to mass diffusivity, called the Lewis number, is equal to unity.

2.4.1.3. Non-linear relation

Even if the linear relation has been extensively adopted in various studies concerning flame propagation (Beckmann et al., 2019; Bradley et al., 2019; Ichikawa et al., 2019; Torrado et al., 2017), it has some limitations (Petersen and Emmons, 1961). Indeed, this relation is less accurate for Lewis numbers different from unity (Tien and Matalon, 1991) and if the flame stretching level is high, which corresponds to great values of the Karlovitz factor (Vagelopoulos et al., 1994). As a consequence, some authors developed and applied a nonlinear relation to link the unstretched flame velocity to the flame stretching of gaseous mixtures (Buckmaster, 1977; Halter et al., 2010; Kelley and Law, 2009; Sivashinsky, 1975):

$$\left(\frac{S_u}{S_u{}^0}\right)^2 . ln\left(\frac{S_u}{S_u{}^0}\right)^2 = -\frac{2\delta_M K}{S_u{}^0} \quad (5)$$

The previous analysis was applied along with relations 4 and 5 to the experimental data recorded during flame propagation in the semi-open tube and in the vented 20L sphere.

2.4.1.4.Estimation of the unstretched burning velocity

An illustration of the evolution of the burning velocity with the Karlovitz factor is presented in Figure 4 for a concentration of 500 $g.m^{-3}$ of nanocellulose. It appears that both relations seem to match approximately the experimental data. In this example, the unstretched flame velocity obtained using the linear relation is 20.5 ± 0.6 $cm.s^{-1}$ and 21.3 ± 0.6 $cm.s^{-1}$ using the nonlinear relation proving a good consistency between both methods. It should be noted that the average discrepancy between the flame velocities obtained by both methods is 4 %, which

means that there is no statistical difference between the methods. However, it appears in Figure 4 that the scattering of data is far from being negligible, which is notably due to uncertainties in the flame surface determination at each step of the propagation and hinders sometimes the application of such correlation.

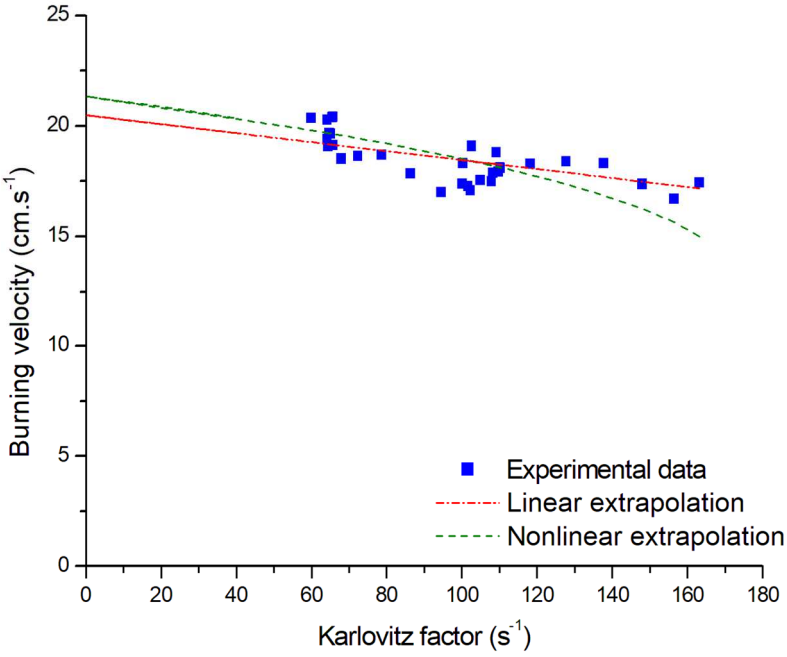

Figure 4. Illustration of the burning velocity – stretching factor relation for a 500 g.m^{-3} nanocellulose-air mixture for tv = 340 ms

Since the derivation process used to determine the Karlovitz factor and the spatial velocity can induce some uncertainties, the time evolution of the position of the flame front, the flame area and cross-section was systematically smoothed based on a second order polynomial as shown in Figure 5 to obtain a general trend and avoid local discontinuities. The coefficient of determination is systematically at least 0.99, showing a good agreement with the experimental results.

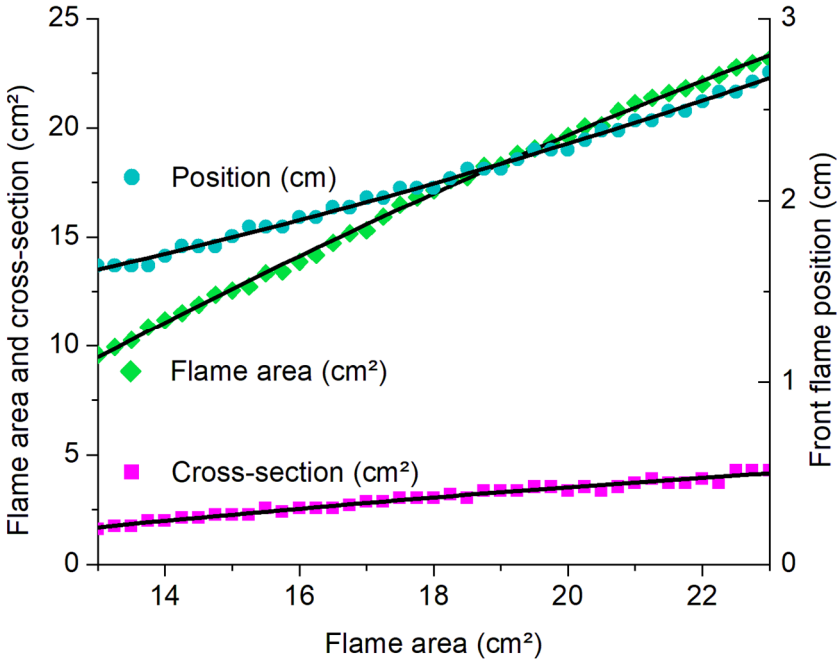

354

355 *Figure 5. Evolution of the front flame position, flame area and cross-section with time for a*

356 *500 g.m^{-3} nanocellulose-air mixture for tv = 340 ms*

357 Figure 6 then represents the evolution of the burning velocity with the stretching factor after
358 data smoothing, showing a better agreement with the different theoretical relationships than
359 the initial raw experimental data. Indeed, the unstretched burning velocity now reaches 23.1 ±
360 0.3 cm.s^{-1} with a coefficient of determination of 0.95 instead of 0.36 in the previous case with
361 the linear fitting, and it reaches 21.8 ± 0.4 cm.s^{-1} using the nonlinear fitting. Since the
362 smoothing provides results with a better accuracy, it was systematically realized during the
363 videos analysis phase.

364 Videos of the explosion occurring in the flame propagation tube and in the vented 20L sphere
365 were then analyzed according to the method described in 2.4.1 and the unstretched burning
366 velocity was estimated using both linear and nonlinear relations.

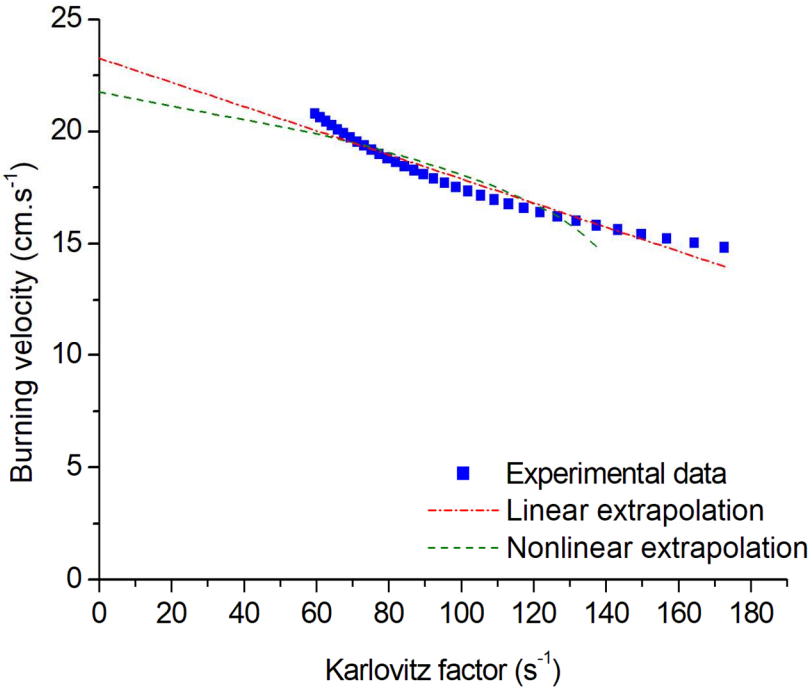

Figure 6. Illustration of the burning velocity – stretching factor relation after smoothing for a 500 g.m^{-3} nanocellulose-air mixture for tv = 340 ms

2.4.2. Pressure-time evolution interpretation

An alternative way to estimate the unstretched burning velocity is provided through the recording of the pressure evolution during an explosion in the 20L sphere. Indeed, some authors such as Silvestrini et al. (2008) developed some correlations between the unstretched burning velocity and the parameters K_{St} and P_{max} obtained in the 20L sphere. The results obtained by analyzing the flame propagation will be compared to the ones calculated from the following semi-empiric correlation defined by Silvestrini et al. (2008):

$$S_u{}^0 = 0.11 \frac{K_{St}}{P_{max}\left(\frac{P_{max}}{P_0}\right)^{0.14}\left(\frac{P_{max}}{P_0}\right)^{\left(\frac{1}{\gamma}\right)}} \quad (6)$$

where P_0 is the atmospheric pressure and γ the ratio of specific heats. As the previously defined relations, this correlation is based on several assumptions, such as the spherical

expansion of the flame and the neglecting of the turbulent length scales. Moreover, the establishment of this correlation based on other existing relations also relying on hypotheses, like a laminar flow or the fact that the burnt gases are trapped behind the expanding flame front, meaning the thermal expansion factor is considered (Harris, 1983). Furthermore, the explosivity index K_{St} is mentioned in the correlation, meaning that the "cube-root" law and its related hypotheses were used. For instance, the flame front is considered to be a thin reaction zone as defined by Dahoe et al. (1996), and Silvestrini et al. (2008) considered that P_{max} was defined as the maximum overpressure for a single explosion experiment and that a Kst parameter can be defined from a test performed at a single dust concentration and not from tests performed over a wide range of concentration. Thus, the following relation was applied during this work:

$$S_u{}^0 = 0.11 \frac{\left(\frac{dP}{dt}\right)_m V^{1/3}}{P_m \left(\frac{P_m}{P_0}\right)^{0.14} \left(\frac{P_m}{P_0}\right)^{\left(\frac{1}{\gamma}\right)}} \quad (7)$$

The unstretched burning velocity of nanocellulose was then estimated using those three methods to test the strengths and weaknesses of each method and ensure the consistency of the methods by identifying a reliable value of the laminar burning velocity.

3. Results and discussion

3.1. Particle size distribution of the dust cloud

When characterizing the dust cloud, it first appears that the particle size distribution in the sphere seems to be more monodisperse than in the tube due to the high shear stress occurring during the injection of the powder and potentially breaking the agglomerates of a few micrometers (Figure 7). Although particles with a diameter lower than 0.5 µm seem to be present in the flame propagation tube and probably in the sphere, they are not measured directly with this lens.

Similar tests were also performed with the same sensor equipped with a R1 lens (from 0.1 to 35 µm). In addition, the PSD of the dust clouds was investigated using a Fast Mobility Particle Sizer (FMPS) and a Scanning Mobility Particle Sizer (SMPS) to specifically measure particles with diameters lower than 500 nm in the 20L sphere. It should be underlined that such apparatuses allow the determination of the electrical mobility distribution of the dust cloud. Although it is impossible with those methods to directly compare the PSD of the dust in the sphere and the tube, these experiments clearly confirm the presence of nanoparticles after dispersion in both equipment with dimensions ranging from 100 to 300 nm (with peaks at 150 nm).

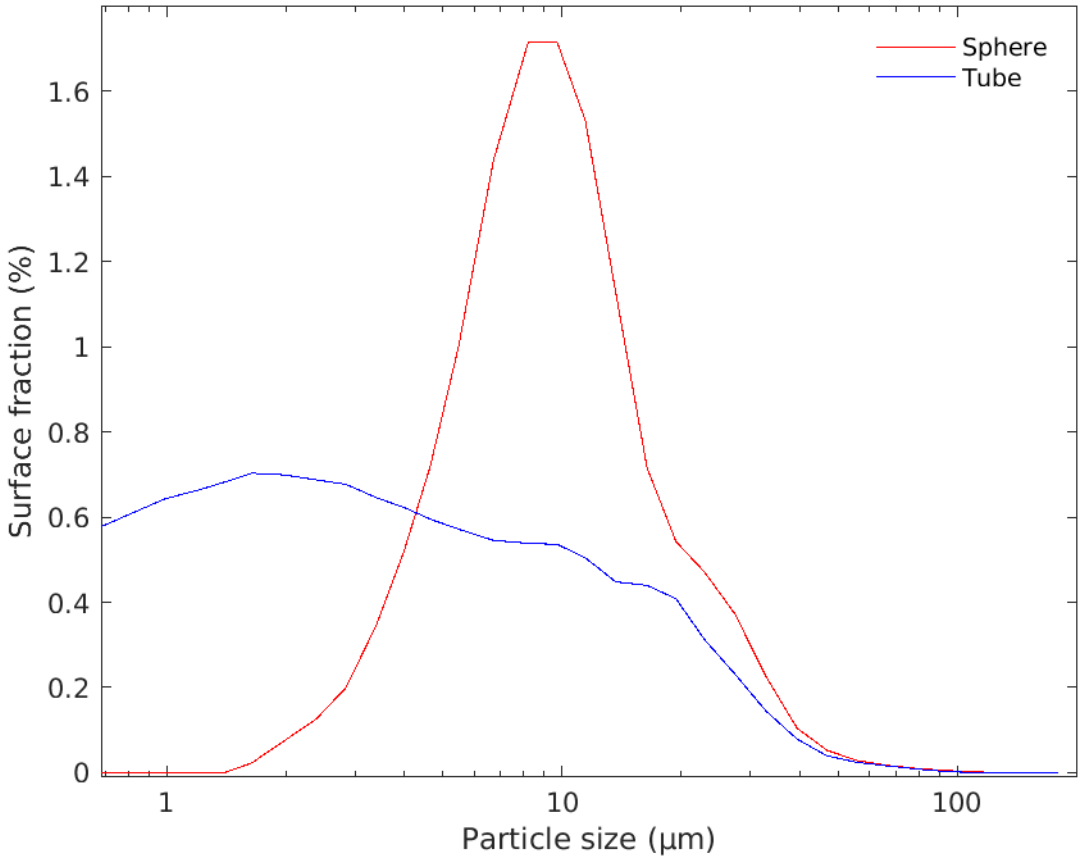

Figure 7. Evolution of the particle size distribution of nanocellulose agglomerates 200 ms after dispersion in the 20L sphere and in the tube at the ignition location

3.2. Explosion severity of micro and nanocellulose

Before proposing an alternative method for dust explosivity assessment, the standard test method (EN 14034) was applied to compare the explosion severity of micro and nanocellulose. It can be observed that the maximum overpressure P_m (Figure 8a) of the nanocellulose is slightly greater than that of microcrystalline cellulose, but that the overall behavior of this parameter as a function of the dust concentration is rather similar for both compounds. However, the difference is more significant with respect to the maximum rate of pressure rise $(dP/dt)_m$ (Figure 8b), which can be explained by the variation of particle size and of specific surface area, which greatly impacts the reaction kinetics. The K_{st} parameter, obtained through the application of the cubic law, reaches 135 ± 3 bar.m.s^{-1} for nanocellulose at 1000 g.m^{-3}, whereas it reaches only 86 ± 10 bar.m.s^{-1} at 1500 g.m^{-3} for microcrystalline cellulose.

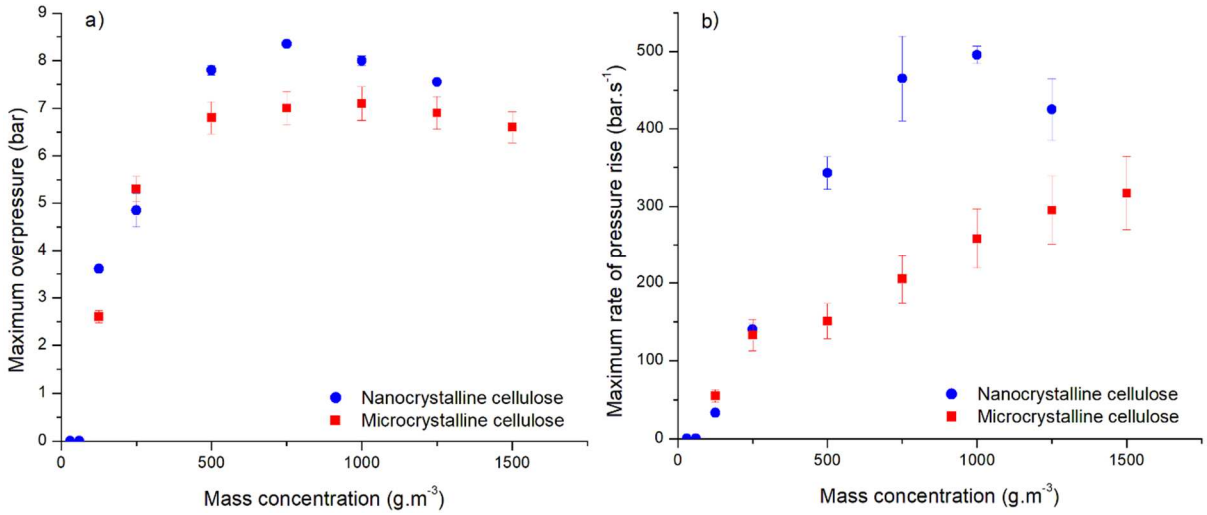

Figure 8. a) Maximum overpressure and b) maximum rate of pressure rise of nanocellulose and microcellulose in standard test conditions

3.3. Determination of the optimal operating conditions for flame propagation tests

Explosion tests were first performed at different ignition delay times and at a single concentration of 500 g.m^{-3}, estimated in the tube by considering the dust weight and an average dispersion height of 0.35 cm. This concentration is close to the stoichiometric

concentration (around 250 $g.m^{-3}$) and ensures a visualization of the flame kernel without interference coming from the particles, which occurs with larger concentrations. At high turbulence, i.e. at an ignition delay time lower than 200 ms, the flame kernel grows up rapidly with stretching and is rapidly influenced by the walls (Figure 9a). As a consequence, only a few milliseconds of the video are suitable for the analysis, and the flame profile is difficult to identify due to the turbulence. When slightly reducing the turbulence, the flame kernel growth is slower, but the turbulence level remains too decisive ($u_{rms} > 1$ $m.s^{-1}$) to precisely define the flame profile (Figure 9b). At very low turbulence, the flame kernel growth is still slow and nearly spherical, showing a behavior similar to that of gases, i.e. a rather smooth flame surface and a flame front with a paraboloidal shape (Figure 9c). It is then possible to correctly identify the flame profile, with 10 to 20 ms of video which can be confidently analyzed. Moreover, it can be noticed that the flame kernel does not move when growing, which shows that it is barely affected by the dust cloud inertia or by the burnt gases thrust. As a result of these observations, ignition delay times from 300 ms to 450 ms, due to a limitation of the apparatus, were considered in the tube and in the 20L sphere for the analyses.

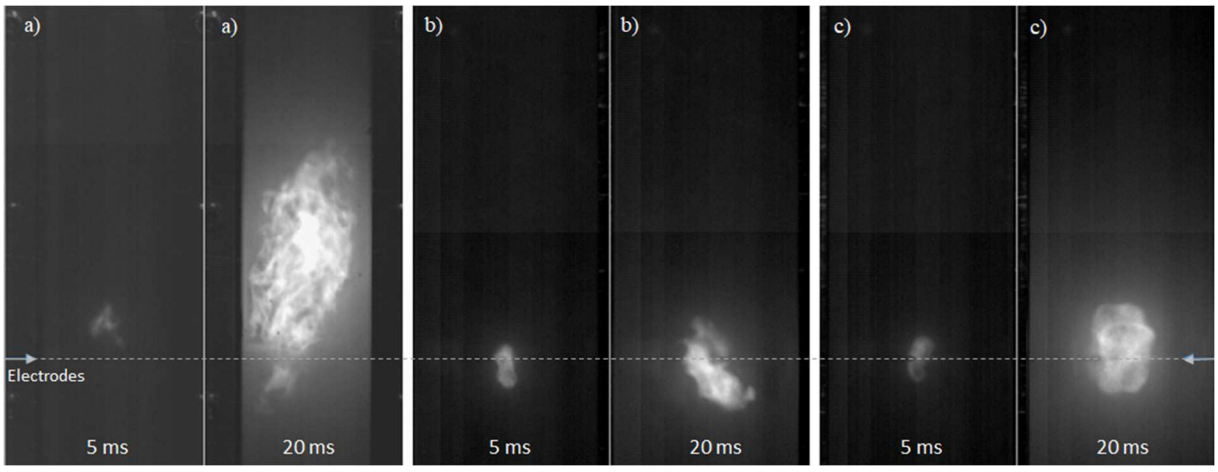

Figure 9. Visualization of flame propagation of 500 $g.m^{-3}$ of nanocellulose in the tube 5 ms and 20 ms after ignition for different ignition delay times (a) 125 ms (b) 235 ms (c) 450 ms.

Figure 10 presents the results obtained in the flame propagation tube and in the open 20L sphere at different ignition delay times, calculated by linear and nonlinear relations. It appears in Figure10a that unstretched burning velocities between 18 and 23 $cm.s^{-1}$ are obtained using the linear equation and that velocities ranging between 17.5 and 26 $cm.s^{-1}$ are obtained with the nonlinear relation, which remains in the same order of magnitude. Both methods lead to similar values, even if the dispersion of the experimental data seems to be more significant in the case of the nonlinear equation. Moreover, Figure 10b shows that the analytical uncertainties are higher when applying the nonlinear relationship to the experimental data measured in the open 20L sphere.

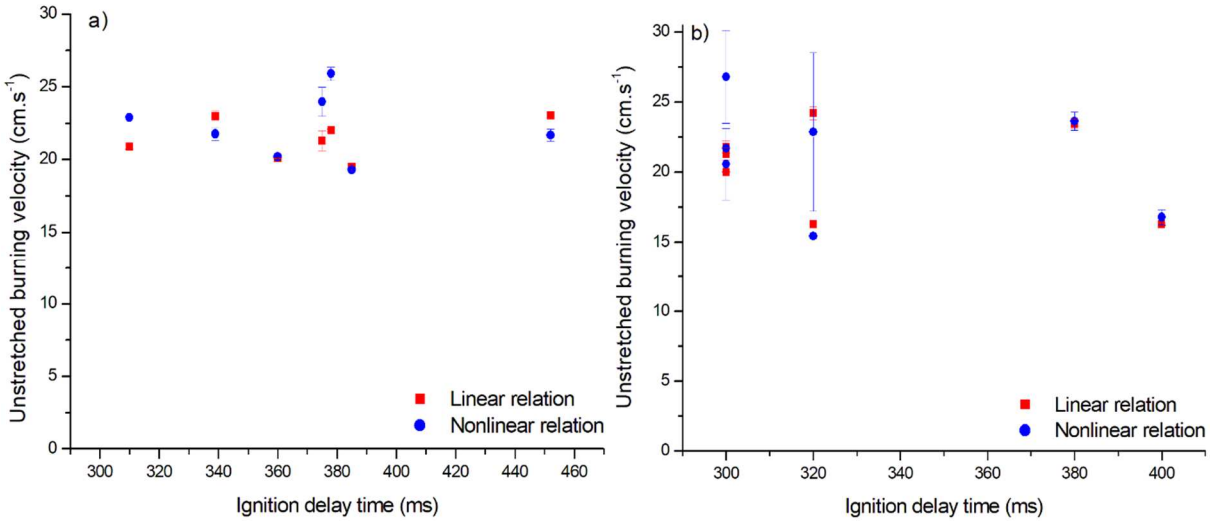

Figure 10. Evolution of the unstretched burning velocity of 500 $g.m^{-3}$ of nanocellulose with ignition delay time calculated by the linear and nonlinear relations in a) the propagation tube b) the open 20L sphere

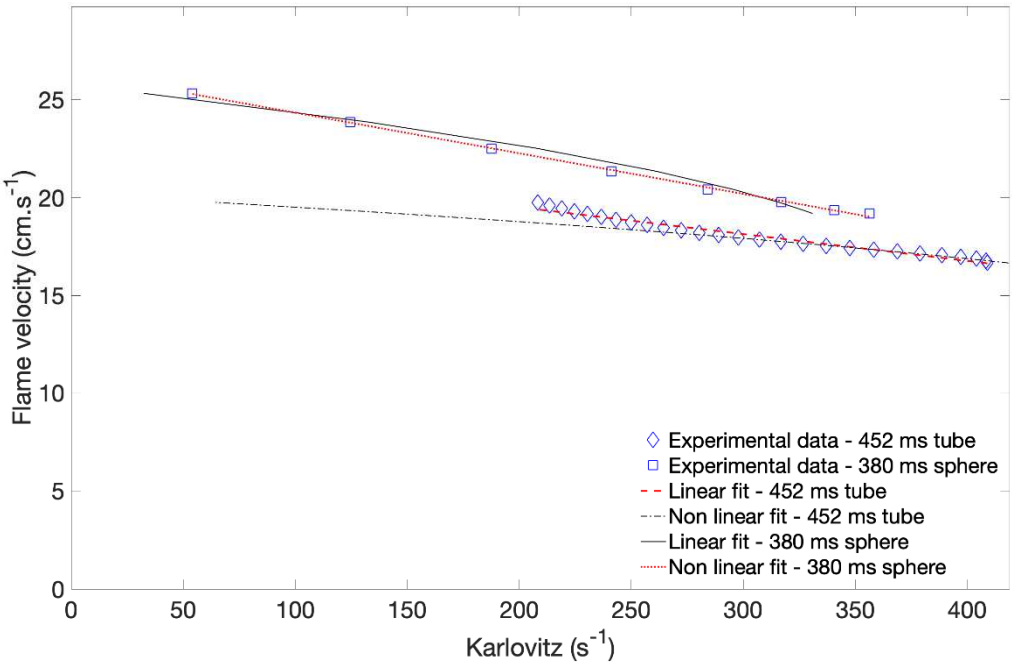

468

469 *Figure 11. Comparison of the application of linear and nonlinear methods to a nanocellulose*

470 *explosion: 500 g.m^{-3}concentration, tv=452 ms – tube and tv=380 ms – vented sphere*

471

472 Figure 11 shows that the application of the nonlinear relationship is more relevant for the
473 experimental data corresponding to the high-stretch region (from 270 to 400 s^{-1}) of the flame
474 propagation in the tube. However, this zone corresponds to a period of time during which the
475 flame propagation may still be affected by the ignition (near 400 s^{-1}). In most cases, as for
476 instance for the other experimental set of data presented in Figure 11 (380 ms in the open
477 sphere), the linear fit will be preferred to the nonlinear model, especially at low stretching
478 rates. It can also be observed in Figure 11 that the number of experimental points selected for
479 the analysis is often reduced in the case of the open sphere. Indeed, with regard to the tube,
480 the larger volume of the 20 L open sphere is both an advantage and a drawback: an advantage
481 because it reduces the wall effects and a drawback because, during the very first moments of
482 the flame kernel growth, the thickness of the unburnt cloud located between the ignition zone

and the window is great, which hinders the flame visualization and sometimes reduces the 'analyzable duration' of the video down to 5 ms. This limitation can be partially overcome by using a Schlieren system, as presented in paragraph 2.2. An explosion in the 20L sphere and the dust kernel 5 ms and 10 ms after ignition of 500 $g.m^{-3}$ of nanocellulose are presented in Figure 12a and Figure 12b respectively. In view of the experimental uncertainties and the slight discrepancies between the non-linear and linear relationships, only the results obtained by the latter method will be now considered.

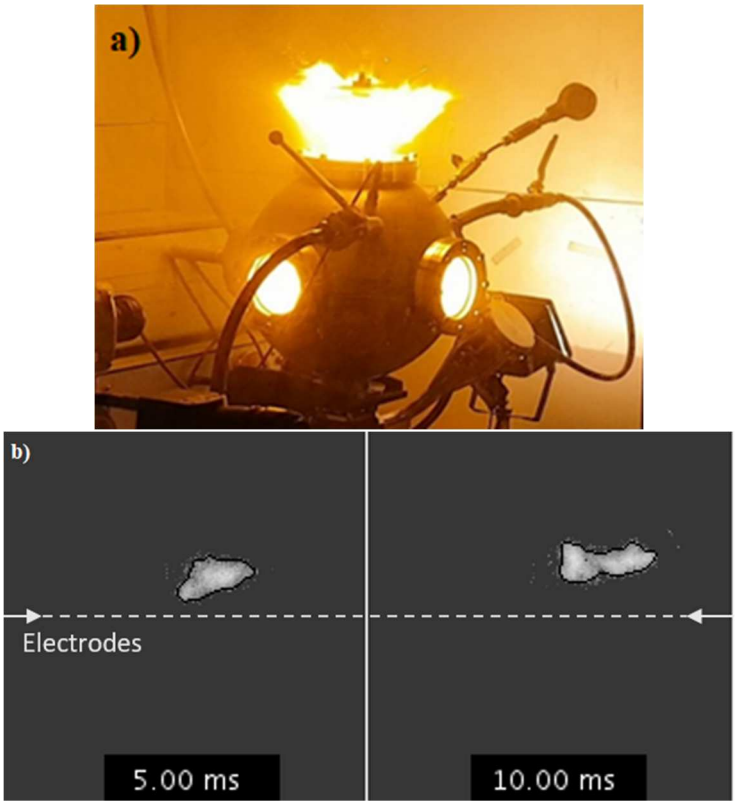

Figure 12. a) Explosion in the open 20L sphere and b) visualization of the flame kernel 5 ms and 10 ms after ignition of 500 $g.m^{-3}$ of nanocellulose and ignition delay time of 300 ms

3.4.Estimation of the laminar burning velocity

Since the turbulence intensity is different in the tube and in the sphere, results were plotted as a function of the root mean square velocity measured in both equipment by Particle Image

Velocimetry. Figure 13 then shows that a very low turbulence level, from 0.21 to 0.13 $m.s^{-1}$ is reached in the tube, whereas it reaches a minimum of 0.3 $m.s^{-1}$ in the 20L sphere. However, similar values of unstretched burning velocity are obtained, from 19 to 23 $cm.s^{-1}$ in the tube and from 16 to 24 $cm.s^{-1}$ in the sphere. This is due to the fact that, when increasing the ignition delay time, the turbulence level decreases in both equipment until it reaches a region in which the decay is small, as mentioned in paragraph 2.3. This region is observed from 200 ms in both equipment, corresponding to a root-mean square velocity of 0.4 $m.s^{-1}$ in the propagation tube and 0.5 $m.s^{-1}$ in the 20L sphere. The flame propagation tube seems to produce more clustered values, which can be explained by the better visualization of the flame kernel providing a longer analyzable video than in the vented 20L sphere, thus a more accurate analysis of the flame propagation.

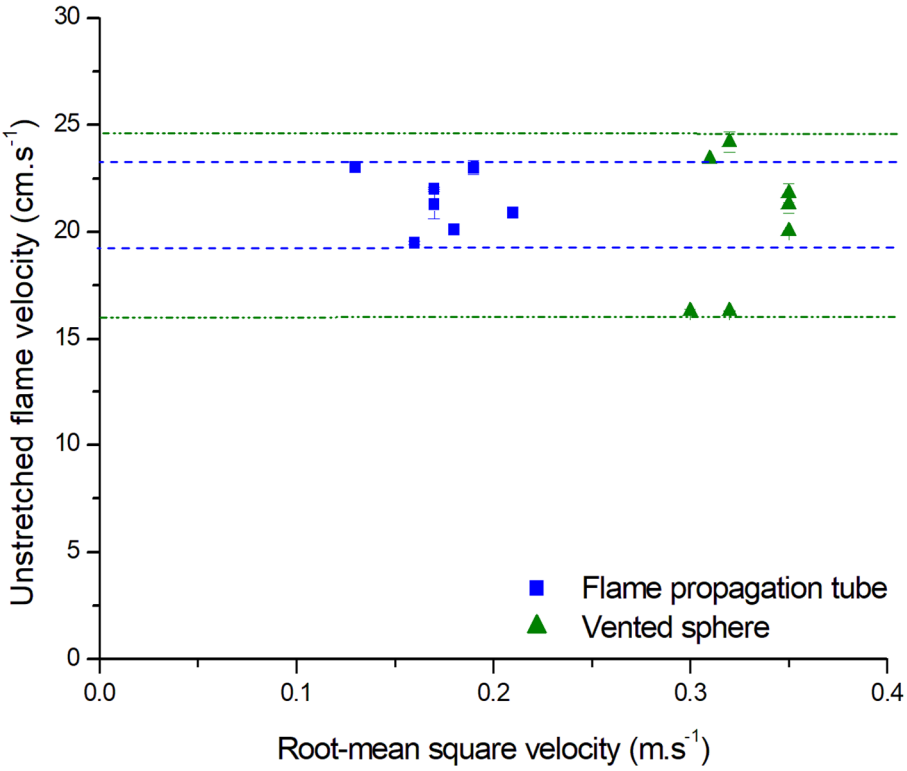

Figure 13. Evolution of the unstretched burning velocity with the root mean square velocity in the flame propagation tube and in the open 20L sphere

514 The values of the unstretched burning velocities obtained through visualization of the flame
515 propagation were then compared to the value acquired by pressure-time recording in the
516 standard 20L apparatus (Figure 14). Using the semi-empirical correlation previously detailed
517 (Equation 7), an unstretched burning velocity of 19.9 $cm.s^{-1}$ is obtained at a root mean square
518 velocity of 3.5 $m.s^{-1}$ while the same value was reached in the flame propagation tube and
519 vented 20L sphere for root mean square velocities of 0.2 $m.s^{-1}$ and 0.3 $m.s^{-1}$ respectively. This
520 is due to the fact that the empirical coefficient of the correlation was established by
521 considering explosion tests performed in standard conditions in the 20L sphere. The equation
522 was applied with a coefficient 0.11 as proposed by the authors, but it makes it valid only for
523 $(dP/dt)_m$ and P_m obtained with an ignition delay time of 60 ms, i.e. a root-mean square
524 velocity of 3.5 $m.s^{-1}$, as previously presented in Table 1.

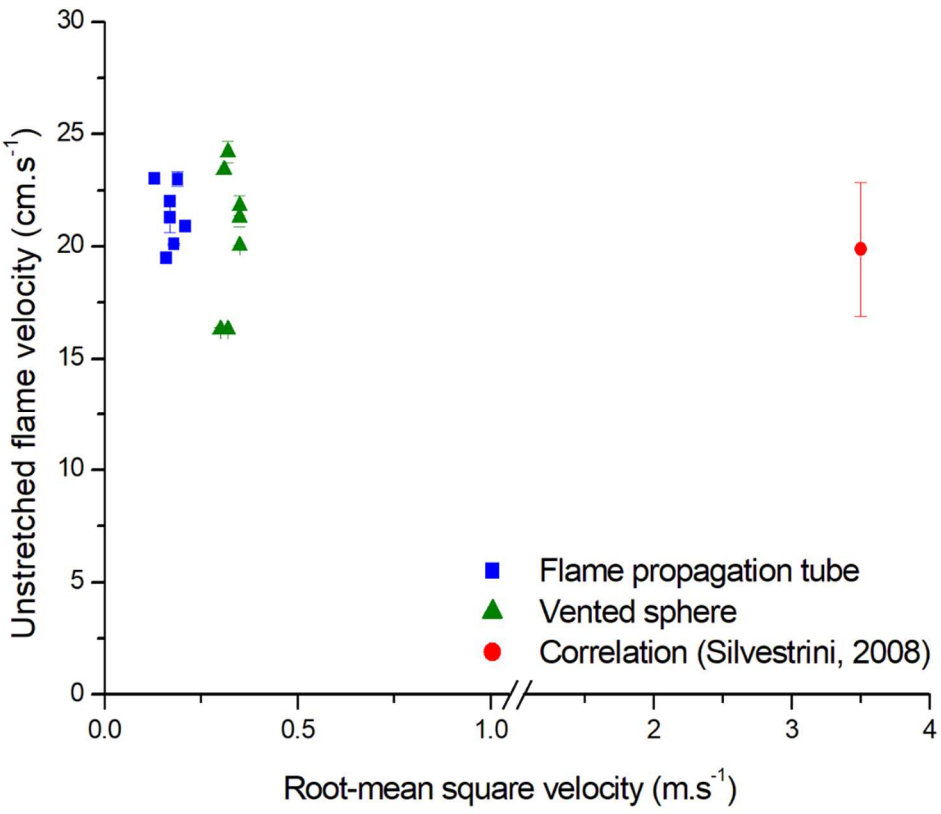

525

526 *Figure 14. Evolution of the unstretched burning velocity with the root mean square velocity*
527 *measured in the flame propagation tube, the vented 20L sphere and the standard 20L sphere*

The laminar burning velocity was then calculated by application of Silvestrini's correlation (eq. 6) to the parameters P_m and $(dP/dt)_m$ obtained with a standard explosion in the 20L sphere, with an ignition energy of 10J and ignition delay time of 60 ms. Moreover, since Cuervo (2015) and Dahoe et al. (2001) showed that the vertical velocity of the particles is close to zero for ignition delay times greater than 300 ms in the propagation tube and in the 20L sphere, and since the flame kernel stays put when growing, the flame propagation visualized in both equipment is considered to be independent of the turbulence level, and the laminar burning velocity was then estimated by averaging the measured values of unstretched burning velocities. However, in addition to the difficulties to identify the flame kernel in the vented sphere, significant fluctuations in the velocity in the sphere can explain the more important scattering of the values of the unstretched burning velocities obtained compared to the ones obtained in the tube. The values of laminar burning velocity of the nanocellulose determined for each method are presented in Table 2.

Table 2. Laminar burning velocity of the nanocellulose estimated by the three different methods

Method	*Flame propagation tube (flame visualization)*	*Open 20L sphere (flame visualization)*	*Standard 20L sphere (pressure evolution)*
Laminar burning velocity ($cm.s^{-1}$)	21.4 ± 1.4	20.5 ± 3.2	19.9 ± 3.0

It first appears that the three methods lead to similar results, the propagation tube providing the less scattered values of laminar burning velocity. The calculation performed using Silvestrini et al. (2008) correlation also provides a value in good agreement with the values measured by flame propagation analysis, but with a higher uncertainty than in the propagation

551 tube. It is mainly due to the lack of reproducibility of the experiments in the standard 20L
552 sphere at 60 ms (Proust et al., 2007). Indeed, at an ignition delay time of 60 ms, the turbulence
553 level is in the "transition stage" identified by Murillo et al. (2018), and turbulence variations
554 have a strong impact on the maximum rate of pressure rise. Adapting the correlation with a
555 coefficient estimated from experiments performed in pseudo-laminar conditions, i.e. higher
556 ignition delay time, would then improve the accuracy of the estimation of the laminar burning
557 velocity. It would then be interesting to use flame propagation analysis on different powders
558 to determine such a coefficient and to apply it to the correlation established by Silvestrini et
559 al. (2008). However, this adapted correlation would have to be used with P_m and $(dP/dt)_m$
560 measured in the same turbulent conditions than the coefficient, which can limit the application
561 of such a relation. To apply this correlation to different conditions and represent industrial
562 situations, an evaluation of the evolution of the correlation coefficient with the initial
563 turbulence is then required.

564 Since the correlation has been validated for nanocellulose at 60 ms, a first estimation of the
565 coefficient dependency with the turbulence was realized through explosion tests conducted in
566 the standard closed 20L vessel by varying the ignition delay time from 60 ms to 300 ms. By
567 applying the correlation used previously and considering the value obtained at 60 ms as a
568 reference, the corrected correlation coefficients were estimated for different root-mean square
569 velocities, as presented in Figure 15. It appears that the value to consider to obtain the laminar
570 burning velocity of 19.9 $cm.s^{-1}$ increases when decreasing the root-mean square velocity,
571 reaching 0.28 at 0.4 $m.s^{-1}$, i.e. more than twice the initial value of 0.11 at 3.5 $m.s^{-1}$. The
572 correlation coefficient follows the same evolution as the time after dispersion with the root-
573 mean square velocity, which implies that it could be correlated by a decay law similar to the
574 one established by Dahoe et al. (2001) relating the root-mean square velocity and the time.
575 The determination of such a relation, coupled with a correlation linking the evolution of

576 $(dP/dt)_m$ with the initial turbulence, could then enable an accurate determination of the
577 laminar burning velocity in the closed 20L sphere.

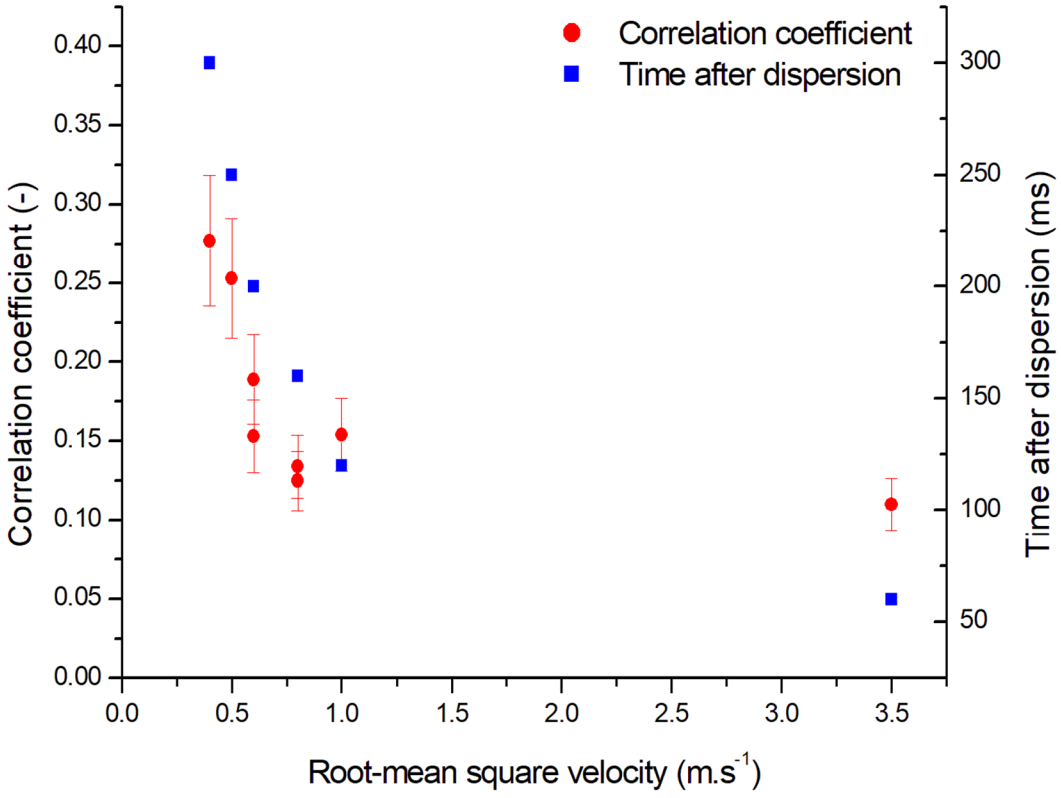

578

579 *Figure 15. Evolution of the time after dispersion and the coefficient from Silvestrini's*
580 *correlation with the root-mean square velocity in the 20L sphere*

581

582 Krause and Kasch (2000) reported laminar burning velocities presented in the literature for
583 different concentrations of two organic powders: lypocodium and cornstarch. Values from 17
584 $cm.s^{-1}$ to 69 $cm.s^{-1}$ were then obtained for lycopodium, and velocities between 13 $cm.s^{-1}$ and
585 59 $cm.s^{-1}$ were acquired for cornstarch. More specifically, van der Wel (1993) reported a
586 laminar flame velocity for cornstarch of 13 $cm.s^{-1}$ at 400 $g.m^{-3}$ using the 20L sphere coupled
587 with a correlation based on Mallard and Le Chatelier thermal theory, and 13 to 20 $cm.s^{-1}$
588 using the burner method for concentrations from 400 $g.m^{-3}$ to 600 $g.m^{-3}$. Haghiri and Bidabadi
589 (2010) also calculated laminar burning velocities for organic powders from 15 $cm.s^{-1}$ to 45

590 cm.s^{-1} for concentrations from 30 g.m^{-3} to 100 g.m^{-3} using a model considering the thermal
591 radiation effect. Moreover, Cuervo et al. (2017) also measured a laminar burning velocity for
592 915 g.m^{-3} of starch around 19.9 cm.s^{-1}. Since starch and nanocellulose have similar structures
593 and composition, these values are in good agreement with the value of 21.4 cm.s^{-1} obtained in
594 the tube for the nanocellulose, despite the different concentrations.

595 The Markstein length was also calculated from video analysis of the flame propagations in the
596 tube and the vented sphere. Similar values were obtained in both equipment, with a mean
597 value of -0.25 mm in the propagation tube and -0.19 mm in the vented sphere. A negative
598 value of the Markstein length means that the flame speed increases with the stretch rate,
599 implying that the flame is unstable. However, the obtained values are very low (absolute
600 values usually lower than 1 mm), and some positive values up to 0.3 mm were also obtained
601 when analyzing the flame propagation videos under certain conditions, which makes it
602 difficult to draw an accurate conclusion on the Markstein length of nanocellulose flames.
603 Nevertheless, it should be stressed that these values are much lower than that obtained by
604 Dahoe et al. (2002) for cornstarch-air mixtures, i.e. 11.0 mm, but are a bit higher than those
605 encountered for methane-air mixtures, i.e. from 0.1 to 0.2 mm. This can be related to the fact
606 that nanocellulose is prone to devolatilization when exposed to high temperatures.

607 3.5. Influence of the dust concentration

608 Even though the theoretical stoichiometric concentration for the combustion of nanocellulose
609 is of approximately 250 g.m^{-3}, it appears in Figure 8 that the most severe explosions were
610 obtained for concentrations of 750 g.m^{-3} and 1000 g.m^{-3} in terms of maximum overpressure
611 and maximum rate of pressure rise. It is then legitimate to investigate the influence of the dust
612 concentration on the laminar burning velocity. However, the estimation of the flame
613 propagation at high concentration is difficult since the dust cloud can hinder the visualization
614 of the flame kernel. A few tests were performed in the flame propagation tube at larger dust

615 concentrations (i.e. 750 g.m^{-3}) and a slight increase of the flame velocity was observed.
616 However, since it is currently impossible to accurately estimate the laminar burning velocity
617 at high concentration using the flame propagation visualization method due to flame
618 obscuring, it was calculated as previously, using the correlation established by Silvestrini et
619 al. (2008) coupled with the standard results presented in Figure 8. It has to be noticed that
620 those experiments were carried out with chemical ignitors of 10 kJ, contrary to the results
621 presented in Figure 14 carried out using an electrical spark of 10 J, which limits the impact of
622 the shock wave created by the igniters.

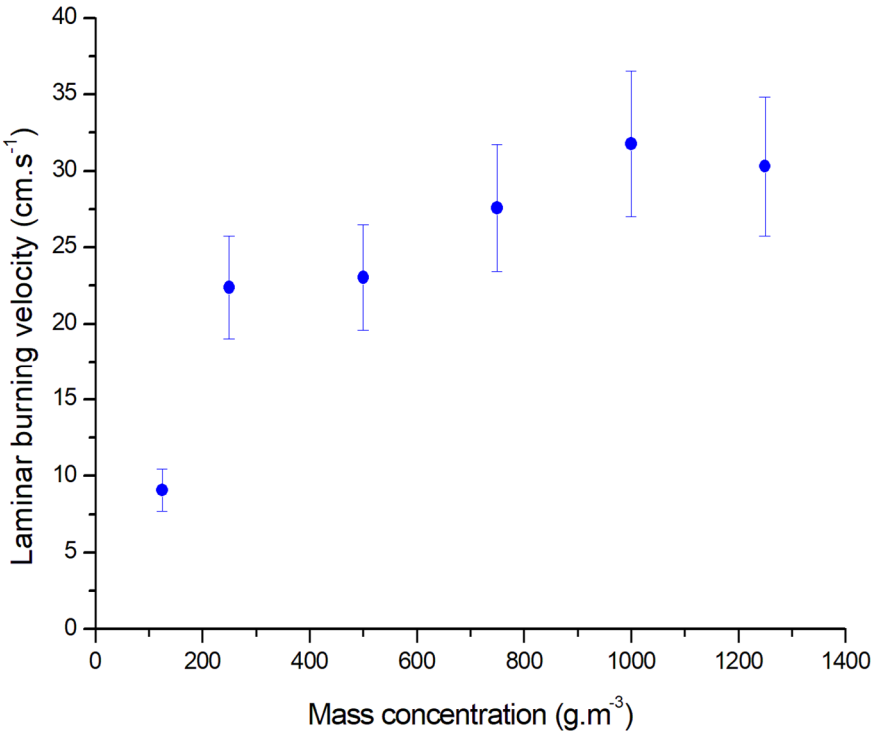

623

624 *Figure 16. Evolution of the laminar burning velocity calculated by a semi-empiric correlation*
625 *with the mass concentration*

626

627 Since the laminar burning velocity is calculated from the knowledge of the maximum
628 overpressure and the maximum rate of pressure rise, it follows the same evolution as those
629 parameters (Figure 16). The maximum value is obtained around 32 cm.s^{-1} for a concentration
630 of 1000 g.m^{-3}. This value is close to the laminar burning velocity of stoichiometric methane

631 generally reported to be around 35 $cm.s^{-1}$ (Bradley et al., 2017) for a maximum overpressure
632 of 7.2 bars and a K_g of 395 $bar.m.s^{-1}$, measured in standard conditions by Torrado et al.
633 (2017a). The value calculated for the nanocellulose with the correlation then seems higher
634 than expected considering its medium explosion severity compared to pure methane, thus
635 questioning the validity of the correlation for high concentrations. Indeed, Silvestrini et al.
636 (2008) have chosen 24 dust-air mixtures to calculate the coefficient for the semi-empiric
637 correlation. However, it should be stressed that, among these mixtures, only 3 dust
638 concentrations were higher than 500 $g.m^{-3}$. The same method considering mixtures with a
639 larger range of concentrations may then extend the validity of the correlation to higher
640 concentrations. Indeed, in order to realize an accurate evaluation of the explosion
641 consequences, the influence of the dust concentration on the laminar burning velocity must be
642 considered. The value corresponding to the worst-case scenario could then be loaded in
643 simulation and by adding the contribution of the turbulence of the dust cloud, the
644 consequences of an explosion in specific conditions can be estimated. It implies that the
645 turbulent burning velocity has to be deduced from the knowledge of the laminar burning
646 velocity and the turbulence level.

647 3.6. Application of turbulent burning velocity models

648 Several correlations relating the turbulent burning velocity to the laminar burning velocity and
649 the turbulence intensity exist in the literature, and were notably summarized by Andrews et al.
650 (1975), Dahoe et al. (2013) and Gülder (1991). Although these models were established for
651 premixed flames, some of the correlations presented by Dahoe et al. (2013) were tested in this
652 study to be compared, in a reverse approach, to the values of turbulent burning velocities
653 obtained by analyzing the flame propagation in the tube (Table 3). In addition to those
654 correlations, the relation established by Popat et al. (1996) used in the FLACS-DustEx CFD

code (relation (g)) was applied to the experimental data produced in this work (Ghaffari et al., 2019; Skjold, 2007).

Table 3. Some turbulent burning velocity models for premixed flame propagation

Notation	Formula	Reference
(a)	$\frac{Su_T}{Su_L} = 1 + \frac{u_{rms}}{Su_L}$	(Damkoehler, 1947)
(b)	$\frac{Su_T}{Su_L} = \sqrt{1 + \left(\frac{u_{rms}}{Su_L}\right)^2}$	(Shelkin, 1947)
(c)	$\frac{Su_T}{Su_L} = 1 + \sqrt{\frac{5}{12}}\frac{u_{rms}}{Su_L}$	(Taylor, 1922)
(d)	$\frac{Su_T}{Su_L} = 1 + \sqrt{2}\left(\frac{u_{rms}}{Su_L}\right)^{1/2}$	(Taylor, 1922)
(e)	$\frac{Su_T}{Su_L} = \sqrt{1 + \left(\frac{2\,u_{rms}}{Su_L}\right)^2}$	(Leason, 1951)
(f)	$\frac{Su_T}{Su_L} = 1 + \left(\frac{u_{rms}}{Su_L}\right)^2$	(Clavin and Williams, 1979)
(g)	$Su_T = 15.1\, {Su_L}^{0.784}\, {u_{rms}}^{0.412}\, {l_i}^{0.196}$	(Popat et al., 1996)

Concerning the models mentioned by Dahoe et al. (2013), it appears in Figure 17 that an average difference of 55% is observed between the model providing the best fitting, i.e. model (d) from Taylor (1922), and experimental data, meaning none of the models actually fits the experimental data. This statement is not only related to the fact that correlations established for premixed flame were applied to a diffusional flame, since it was previously underlined for premixed flames of methane-air and hydrogen-air mixtures by Dahoe et al. (2013), who then proposed a semi-empiric correlation of the following form :

$$\frac{Su_T}{Su_L} = 1 + a_1\, {D_a}^{a_2} \left(\frac{u_{rms}}{Su_L}\right)^{a_3} \quad (8)$$

667 a_1, a_2 and a_3 being three coefficients to determine experimentally and Da the Damköhler
668 number. They observed that two distinct sets of coefficients exist in their operating
669 conditions, revealing that the establishment of a unique correlation allowing the calculation of
670 the turbulent burning velocity from the knowledge of the laminar burning velocity and the
671 turbulence intensity is not trivial, even for gases.

672 The model established by Popat et al. (1996) and considered in the CFD code used by Skjold
673 (2007) clearly provides the best fitting with the experimental data from this work, with an
674 average difference of 20%. The difference can be due to experimental uncertainties, notably
675 concerning the point at Su_T/Su_L = 6.8, but also to the different assumptions concerning the
676 correlation, such as a constant kinematic viscosity and the integral length scale l_i equal to 1
677 cm (Skjold, 2003). A proper estimation of the turbulent velocity being essential to provide an
678 accurate risk assessment concerning the consequences of an explosion, further investigations
679 on such models is required.

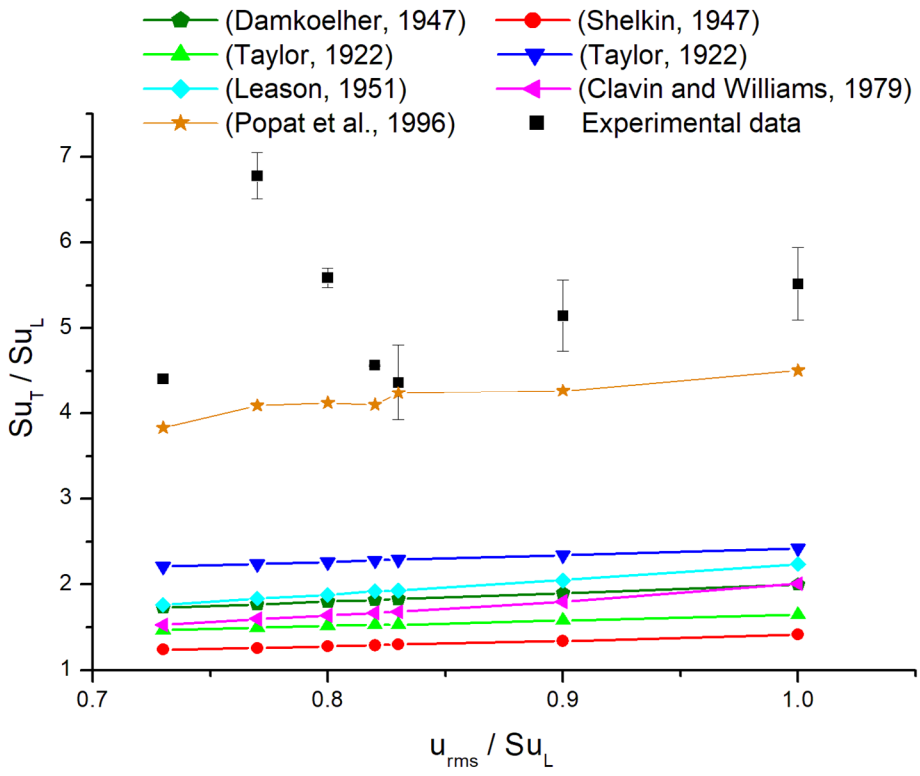

680

681 *Figure 17. Comparison between models listed in Table 3 and experimental turbulent burning*
682 *velocities measured in the flame propagation tube*

683

684 **4. Conclusion**

685 The laminar burning velocity of nanocellulose has been assessed by three different methods
686 including the direct visualization of the flame propagation in a vertical 1 m long tube or in a
687 vented 20L sphere coupled with the application of relationships relating the flame speed and
688 its stretching, and the use of correlations based on the pressure time evolution during a
689 standard explosion test. Both visualization methods, tube or open sphere, lead to similar
690 results, consistent with the values previously presented in the literature for other organic
691 powders, validating this experimental approach for organic powders. Moreover, these results
692 were compared with those obtained from standard tests in the 20L sphere using a semi-
693 empiric correlation relating the pressure evolution and the flame velocity. All three methods
694 lead to similar values of nanocellulose-air laminar burning velocity, i.e. approximately 21
695 $cm.s^{-1}$.

696 The use of nanopowders for such analyses allows reaching very low turbulence levels and
697 thus reduces the impact of turbulence on the flame kernel growth, approaching 'pseudo-
698 laminar' conditions. It has notably been underlined that using such flame propagation
699 analyses at low turbulence can support the development of semi-empiric correlations allowing
700 the estimation of the laminar burning velocity from the knowledge of the pressure-time
701 evolution in the standard 20L sphere. The laminar flame velocity being an intrinsic property
702 of the dust-air mixture, it is likely that such techniques could be used in addition to
703 standardized tests in the 20L sphere in order to increase the scope of their results. Indeed,
704 results obtained from standard tests in standards equipment can only be applied to larger
705 enclosures if reliable scaling laws are available. Otherwise, these results are only valid for the

specific operating conditions defined by the standards. But, as previously stated in introduction, the validity of the widespread 'cube-root-law' depends on several limiting assumptions. Therefore, the determination of a laminar burning velocity can help to overcome such limitations by providing an accurate risk assessment independent from the operating conditions.

However, the knowledge of the laminar burning velocity of a mixture is valuable for industrial purposes only if reliable models exist, converting it to a spatial/turbulent burning velocity knowing the turbulent conditions of the cloud. This point is far from being trivial for dusts and some efforts still have to be made in this direction.

Acknowledgments

The authors would like to warmly acknowledge Claire Dazon, Sébastien Bau and Olivier Witschger (INRS – Vandoeuvre-les-Nancy, France) for FMPS measurements and rotative drum tests. They also would like to thank Augustin Charvet (LRGP CNRS-UL) for SMPS measurements as well as David Brunello, Charly Koenig and Christian Blanchard (LRGP CNRS-UL) for their invaluable contributions in experimental setup design. This work was supported financially by the French Ministry for the Ecological and Solidary Transition and The French Ministry for Higher Education and Research.

References

Abitbol, T., Rivkin, A., Cao, Y., Nevo, Y., Abraham, E., Ben-Shalom, T., Lapidot, S., Shoseyov, O., 2016. Nanocellulose, a tiny fiber with huge applications. Current Opinion in Biotechnology, Systems biology - Nanobiotechnology 39, 76–88. https://doi.org/10.1016/j.copbio.2016.01.002

730 Amyotte, P.R., 2014. Some myths and realities about dust explosions. Process Safety and
731 Environmental Protection, Loss Prevention 2013 92, 292–299.
732 https://doi.org/10.1016/j.psep.2014.02.013

733 Amyotte, P.R., Chippett, S., Pegg, M.J., 1988. Effects of turbulence on dust explosions.
734 Progress in Energy and Combustion Science 14, 293–310.
735 https://doi.org/10.1016/0360-1285(88)90016-0

736 Andrews, G.E., Bradley, D., 1972. Determination of burning velocities: A critical review.
737 Combustion and Flame 18, 133–153. https://doi.org/10.1016/S0010-2180(72)80234-7

738 Andrews, G.E., Bradley, D., Lwakabamba, S.B., 1975. Turbulence and turbulent flame
739 propagation—A critical appraisal. Combustion and Flame 24, 285–304.
740 https://doi.org/10.1016/0010-2180(75)90163-7

741 Bartknecht, W., 1989. Dust-explosions: course, prevention, protection. Springer-Verlag.

742 Belerrajoul, M., 2019. Modélisation multi-échelle de la combustion d'un nuage de particules
743 (PhD Thesis). National Polytechnic Institute of Toulouse.

744 Bidabadi, M., Azad, A.V., 2015. Effects of radiation on propagating spherical flames of dust–
745 air mixtures. Powder Technology 276, 45–59.
746 https://doi.org/10.1016/j.powtec.2014.12.044

747 Boilard, S.P., Amyotte, P.R., Khan, F.I., Dastidar, A.G., Eckhoff, R.K., 2013. Explosibility of
748 micron- and nano-size titanium powders. Journal of Loss Prevention in the Process
749 Industries 26, 1646–1654. https://doi.org/10.1016/j.jlp.2013.06.003

750 Bouillard, J., Vignes, A., Dufaud, O., Perrin, L., Thomas, D., 2010. Ignition and explosion
751 risks of nanopowders. Journal of Hazardous Materials 181, 873–880.
752 https://doi.org/10.1016/j.jhazmat.2010.05.094

753 Bradley, D., 2000. Flame Propagation in a Tube: The Legacy of Henri Guenoche.
754 Combustion Science and Technology 158, 15–33.
755 https://doi.org/10.1080/00102200008947325

756 Bradley, D., Chen, Z., Swithenbank, J.R., 1989. Burning rates in turbulent fine dust-air
757 explosions. Symposium (International) on Combustion 22, 1767–1775.
758 https://doi.org/10.1016/S0082-0784(89)80190-0

759 Bradley, D., Lawes, M., Mumby, R., 2017. Burning velocity and Markstein length blending
760 laws for methane/air and hydrogen/air blends. Fuel 187, 268–275.
761 https://doi.org/10.1016/j.fuel.2016.09.032

762 Bradley, D., Lee, J.H.., 1984. . Proceedings of the first international colloquium on the
763 explosibility of industrial dusts 220–223.

764 CelluForce, 2016, Product specification of CelluForce NCV100, CelluForce company,
765 Montreal, Canada.

766 Chen, Z., Ju, Y., 2007. Theoretical analysis of the evolution from ignition kernel to flame ball
767 and planar flame. Combustion Theory and Modelling 11, 427–453.
768 https://doi.org/10.1080/13647830600999850

769 Clavin, P., 1985. Dynamic behavior of premixed flame fronts in laminar and turbulent flows.
770 Progress in Energy and Combustion Science 11, 1–59. https://doi.org/10.1016/0360-
771 1285(85)90012-7

772 Clavin, P., Williams, F.A., 1979. Theory of premixed-flame propagation in large-scale
773 turbulence. Journal of Fluid Mechanics 90, 589–604.
774 https://doi.org/10.1017/S002211207900241X

775 Clouthier, M.P., Taveau, J.R., Dastidar, A.G., Morrison, L.S., Zalosh, R.G., Ripley, R.C.,
776 Khan, F.I., Amyotte, P.R., 2019. Iron and aluminum powder explosibility in 20-L and

1- m 3 chambers. Journal of Loss Prevention in the Process Industries 62, 103927. https://doi.org/10.1016/j.jlp.2019.103927

Cuervo, N., 2015. Influences of turbulence and combustion regimes on explosions of gas-dust hydrid mixtures (PhD Thesis). The University of Lorraine, France.

Cuervo, N., Dufaud, O., Perrin, L., 2017. Determination of the burning velocity of gas/dust hybrid mixtures. Process Safety and Environmental Protection 109, 704–715. https://doi.org/10.1016/j.psep.2017.06.009

Dahoe, A.E., Cant, R.S., Pegg, M.J., Scarlett, B., 2001. On the transient flow in the 20-liter explosion sphere. Journal of Loss Prevention in the Process Industries 14, 475–487. https://doi.org/10.1016/S0950-4230(01)00052-3

Dahoe, A.E., Hanjalic, K., Scarlett, B., 2002a. Determination of the laminar burning velocity and the Markstein length of powder–air flames. Powder Technology, Special issue i in Honour of Prof Jimbo 122, 222–238. https://doi.org/10.1016/S0032-5910(01)00419-3

Dahoe, A.E., Hanjalic, K., Scarlett, B., 2002b. Determination of the laminar burning velocity and the Markstein length of powder–air flames. Powder Technology, Special issue i in Honour of Prof Jimbo 122, 222–238. https://doi.org/10.1016/S0032-5910(01)00419-3

Dahoe, A.E., Skjold, T., Roekaerts, D.J.E.M., Pasman, H.J., Eckhoff, R.K., Hanjalic, K., Donze, M., 2013. On the Application of the Levenberg–Marquardt Method in Conjunction with an Explicit Runge–Kutta and an Implicit Rosenbrock Method to Assess Burning Velocities from Confined Deflagrations. Flow, Turbulence and Combustion 91, 281–317. https://doi.org/10.1007/s10494-013-9462-z

Dahoe, A.E., Zevenbergen, J.F., Lemkowitz, S.M., Scarlett, B., 1996. Dust explosions in spherical vessels: The role of flame thickness in the validity of the 'cube-root law.'

800 Journal of Loss Prevention in the Process Industries 9, 33–44.
801 https://doi.org/10.1016/0950-4230(95)00054-2

802 Damkoehler, G., 1947. The Effect of Turbulence on the Flame Velocity in Gas Mixtures.

803 Di Benedetto, A., Garcia-Agreda, A., Dufaud, O., Khalili, I., Sanchirico, R., Perrin, L., Russo,
804 P., 2011. Flame propagation of dust and gas-air mixtures in a tube. Proceedings of the
805 7th Mediterranean Combustion Symposium 12.

806 Di Benedetto, A., Russo, P., 2007. Thermo-kinetic modelling of dust explosions. Journal of
807 Loss Prevention in the Process Industries, Selected Papers Presented at the Sixth
808 International Symposium on Hazards, Prevention and Mitigation of Industrial
809 Explosions 20, 303–309. https://doi.org/10.1016/j.jlp.2007.04.001

810 Di Benedetto, Russo, P., Sanchirico, R., Sarli, V.D., 2013. CFD simulations of turbulent fluid
811 flow and dust dispersion in the 20 liter explosion vessel. AIChE Journal 59, 2485–
812 2496. https://doi.org/10.1002/aic.14029

813 Dufaud, O., Vignes, A., Henry, F., Perrin, L., Bouillard, J., 2011. Ignition and explosion of
814 nanopowders: something new under the dust. Journal of Physics: Conference Series
815 304, 012076. https://doi.org/10.1088/1742-6596/304/1/012076

816 Eckhoff, R.K., 2012. Does the dust explosion risk increase when moving from μm-particle
817 powders to powders of nm-particles? Journal of Loss Prevention in the Process
818 Industries 25, 448–459. https://doi.org/10.1016/j.jlp.2011.11.011

819 Eckhoff, R.K., 2003. Dust Explosions in the Process Industries - 3rd Edition, 3rd ed. Gulf
820 Professional Publishing.

821 EN 14034-1, 2004. Determination of explosion characteristics of dust clouds — Part 1:
822 Determination of the maximum explosion pressure Pmax of dust clouds.

EN 14034-2, 2006. Determination of explosion characteristics of dust clouds — Part 2: Determination of the maximum rate of explosion pressure rise (dp/dt)max of dust clouds.

Frankel, M.L., Sivashinsky, G.I., 1984. On Quenching of Curved Flames. Combustion Science and Technology 40, 257–268. https://doi.org/10.1080/00102208408923809

Ghaffari, M., Hoffmann, A.C., Skjold, T., Eckhoff, R.K., van Wingerden, K., 2019. A brief review on the effect of particle size on the laminar burning velocity of flammable dust: Application in a CFD tool for industrial applications. Journal of Loss Prevention in the Process Industries 62, 103929. https://doi.org/10.1016/j.jlp.2019.103929

Going, J.E., Chatrathi, K., Cashdollar, K.L., 2000. Flammability limit measurements for dusts in 20-L and 1-m3 vessels. Journal of Loss Prevention in the Process Industries 13, 209–219. https://doi.org/10.1016/S0950-4230(99)00043-1

Goroshin, S., Tang, F.-D., Higgins, A.J., Lee, J.H.., 2011. Laminar dust flames in a reduced-gravity environment. Acta Astronautica 68, 656–666. https://doi.org/10.1016/j.actaastro.2010.08.038

Gülder, Ö.L., 1991. Turbulent premixed flame propagation models for different combustion regimes. Symposium (International) on Combustion, Twenty-Third Symposium (International) on Combustion 23, 743–750. https://doi.org/10.1016/S0082-0784(06)80325-5

Haghiri, A., Bidabadi, M., 2010. Modeling of laminar flame propagation through organic dust cloud with thermal radiation effect. International Journal of Thermal Sciences 49, 1446–1456. https://doi.org/10.1016/j.ijthermalsci.2010.03.013

Harris, R.J., 1983. The investigation and control of gas explosions in buildings and heating plant. E. & F.N. Spon in association with the British Gas Corp.

847 Jespen, T., 2016. ATEX—Explosive Atmospheres, Springer Series in Reliability Engineering.
848 Springer International Publishing, Cham. https://doi.org/10.1007/978-3-319-31367-2

849 Joulin, G., Clavin, P., 1979. Linear stability analysis of nonadiabatic flames: Diffusional-
850 thermal model. Combustion and Flame 35, 139–153. https://doi.org/10.1016/0010-
851 2180(79)90018-X

852 Julien, P., Whiteley, S., Soo, M., Goroshin, S., Frost, D.L., Bergthorson, J.M., 2017. Flame
853 speed measurements in aluminum suspensions using a counterflow burner.
854 Proceedings of the Combustion Institute 36, 2291–2298.
855 https://doi.org/10.1016/j.proci.2016.06.150

856 Karlovitz, B., Denniston, D.W., Wells, F.E., 1951. Investigation of Turbulent Flames. J.
857 Chem. Phys. 19, 541–547. https://doi.org/10.1063/1.1748289

858 Kosinski, P., Nyheim, R., Asokan, V., Skjold, T., 2013. Explosions of carbon black and
859 propane hybrid mixtures. Journal of Loss Prevention in the Process Industries 26, 45–
860 51. https://doi.org/10.1016/j.jlp.2012.09.004

861 Krause, U., Kasch, T., 2000. The influence of flow and turbulence on flame propagation
862 through dust-air mixtures. Journal of Loss Prevention in the Process Industries 13,
863 291–298. https://doi.org/10.1016/S0950-4230(99)00062-5

864 Krietsch, A., Scheid, M., Schmidt, M., Krause, U., 2015. Explosion behaviour of metallic
865 nano powders. Journal of Loss Prevention in the Process Industries 36, 237–243.
866 https://doi.org/10.1016/j.jlp.2015.03.016

867 Law, C.K., 2006. Combustion Physics by Chung K. Law [WWW Document]. Cambridge
868 Core. https://doi.org/10.1017/CBO9780511754517

869 Leason, D.B., 1951. Turbulence and flame propagation in premixed gases. Fuel 30, 233–239.

870 Lee, J., Peraldi, O., Knystautas, R., 1993. Microgravity combustion of dust suspension, in:
871 31st Aerospace Sciences Meeting. Presented at the 31st Aerospace Sciences Meeting,
872 American Institute of Aeronautics and Astronautics, Reno,NV,U.S.A.
873 https://doi.org/10.2514/6.1993-714

874 Lewis, B., von Elbe, G., 1987. Combustion, Flames and Explosions of Gases. Elsevier.
875 https://doi.org/10.1016/C2009-0-21751-X

876 Lomba, R., Laboureur, P., Dumand, C., Chauveau, C., Halter, F., 2019. Determination of
877 aluminum-air burning velocities using PIV and Laser sheet tomography. Proceedings
878 of the Combustion Institute 37, 3143–3150.
879 https://doi.org/10.1016/j.proci.2018.07.013

880 Markstein, G.H., 1964. Non-steady flame Propagation. P22, Pergarmon, New York.

881 Mazumdar, A., 2013. Principles and Techniques of Schlieren Imaging Systems.
882 https://doi.org/10.7916/D8TX3PWV

883 McBride, B.J., Gordon, S., 1996. Computer Program for Calculation of Complex Chemical
884 Equilibrium Compositions and Applications II. Users Manual and Program
885 Description. NASA. RP 1311.

886 Miao, J., Leung, C.W., Huang, Z., Cheung, C.S., Yu, H., Xie, Y., 2014. Laminar burning
887 velocities, Markstein lengths, and flame thickness of liquefied petroleum gas with
888 hydrogen enrichment. International Journal of Hydrogen Energy 39, 13020–13030.
889 https://doi.org/10.1016/j.ijhydene.2014.06.087

890 Mittal, M., 2014. Explosion characteristics of micron- and nano-size magnesium powders.
891 Journal of Loss Prevention in the Process Industries 27, 55–64.
892 https://doi.org/10.1016/j.jlp.2013.11.001

Mohan, S., Ermoline, A., Dreizin, E.L., 2012. Pyrophoricity of nano-sized aluminum particles. J Nanopart Res 14, 723. https://doi.org/10.1007/s11051-012-0723-x

Murillo, C., 2016. Experimental and numerical approaches to particles dispersion in a turbulent flow : application to dust explosions (PhD Thesis). Université de Lorraine, France.

Murillo, C., Amín, M., Bardin-Monnier, N., Muñoz, F., Pinilla, A., Ratkovich, N., Torrado, D., Vizcaya, D., Dufaud, O., 2018. Proposal of a new injection nozzle to improve the experimental reproducibility of dust explosion tests. Powder Technology 328, 54–74. https://doi.org/10.1016/j.powtec.2017.12.096

Popat, N.R., Catlin, C.A., Arntzen, B.J., Lindstedt, R.P., Hjertager, B.H., Solberg, T., Saeter, O., Van den Berg, A.C., 1996. Investigations to improve and assess the accuracy of computational fluid dynamic based explosion models. Journal of Hazardous Materials 45, 1–25. https://doi.org/10.1016/0304-3894(95)00042-9

Proust, C., 2006. Flame propagation and combustion in some dust-air mixtures. Journal of Loss Prevention in the Process Industries 19, 89–100. https://doi.org/10.1016/j.jlp.2005.06.026

Proust, C., Accorsi, A., Dupont, L., 2007. Measuring the violence of dust explosions with the "20l sphere" and with the standard "ISO 1m3 vessel": Systematic comparison and analysis of the discrepancies. Journal of Loss Prevention in the Process Industries, Selected Papers Presented at the Sixth International Symposium on Hazards, Prevention and Mitigation of Industrial Explosions 20, 599–606. https://doi.org/10.1016/j.jlp.2007.04.032

915 Pu, Y., Podfilipski, J., Jarosiński, J., 1998. Constant Volume Combustion of Aluminum and
916 Cornstarch Dust in Microgravity. Combustion Science and Technology 135, 255–267.
917 https://doi.org/10.1080/00102209808924160

918 Pu, Y.K., Jarosinski, J., Johnson, V.G., Kauffman, C.W., 1991. Turbulence effects on dust
919 explosions in the 20-liter spherical vessel. Symposium (International) on Combustion,
920 Twenty-Third Symposium (International) on Combustion 23, 843–849.
921 https://doi.org/10.1016/S0082-0784(06)80338-3

922 Santandrea, A., Bonamis, F., Pacault, S., Vignes, A., Perrin, L., Dufaud, O., 2019b. Influence
923 of the Particle Size Distribution on Dust Explosion: How to Choose the Right
924 Metrics? Chemical Engineering Transactions 77, 667–672.
925 https://doi.org/10.3303/CET1977112

926 Santandrea, A., Pacault, S., Perrin, L., Vignes, A., Dufaud, O., 2019a. Nanopowders
927 explosion: Influence of the dispersion characteristics. Journal of Loss Prevention in
928 the Process Industries. https://doi.org/10.1016/j.jlp.2019.103942

929 Shelkin, K.I., 1947. On Combustion in a Turbulent Flow [WWW Document]. Journal of
930 Technical Physics; Volume 13; No. 9-10. URL
931 https://digital.library.unt.edu/ark:/67531/metadc64298/ (accessed 10.16.19).

932 Silvestrini, M., Genova, B., Leon Trujillo, F.J., 2008. Correlations for flame speed and
933 explosion overpressure of dust clouds inside industrial enclosures. Journal of Loss
934 Prevention in the Process Industries 21, 374–392.
935 https://doi.org/10.1016/j.jlp.2008.01.004

936 Skjold, T., 2007. Review of the DESC project. Journal of Loss Prevention in the Process
937 Industries, Selected Papers Presented at the Sixth International Symposium on

938 Hazards, Prevention and Mitigation of Industrial Explosions 20, 291–302.
939 https://doi.org/10.1016/j.jlp.2007.04.017

940 Skjold, T., 2003. Selected aspects of turbulence and combustion in 20-Litre explosion vessel
941 (Master thesis). University of Bergen, Norway.

942 Sundaram, D.S., Puri, P., Yang, V., 2013. Pyrophoricity of nascent and passivated aluminum
943 particles at nano-scales. Combustion and Flame 160, 1870–1875.
944 https://doi.org/10.1016/j.combustflame.2013.03.031

945 Tamanini, F., 1990. Turbulence effects on dust explosion venting. Plant/Operations Progress
946 9, 52–60. https://doi.org/10.1002/prsb.720090111

947 Tang, F.-D., Goroshin, S., Higgins, A., Lee, J., 2009. Flame propagation and quenching in
948 iron dust clouds. Proceedings of the Combustion Institute 32, 1905–1912.
949 https://doi.org/10.1016/j.proci.2008.05.084

950 Taveau, J., Lemkowitz, S.M., Hochgreb, S., Roekaerts, D., 2018. Scaling up the severity of
951 metal dusts deflagrations. Proceedings of the 12th International Symposium on
952 Hazards, Prevention and Mitigation of Industrial Explosions (XII ISHPMIE).

953 Taylor, G.I., 1922. Diffusion by Continuous Movements. Proceedings of the London
954 Mathematical Society 20, 196–212. https://doi.org/10.1112/plms/s2-20.1.196

955 Tolias, I.C., Venetsanos, A.G., 2018. An improved CFD model for vented deflagration
956 simulations – Analysis of a medium-scale hydrogen experiment. International Journal
957 of Hydrogen Energy 43, 23568–23584. https://doi.org/10.1016/j.ijhydene.2018.10.077

958 Torrado, D., 2017. Effect of carbon black nanoparticles on the explosion severity of gas
959 mixtures (PhD Thesis). Université de Lorraine, France.

960 Torrado, D., Buitrago, V., Glaude, P.-A., Dufaud, O., 2017a. Explosions of
961 methane/air/nanoparticles mixtures: Comparison between carbon black and inert
962 particles. Process Safety and Environmental Protection 110, 77–88.
963 https://doi.org/10.1016/j.psep.2017.04.014

964 Torrado, D., Cuervo, N., Pacault, S., Glaude, P.-A., Dufaud, O., 2017b. Influence of carbon
965 black nanoparticles on the front flame velocity of methane/air explosions. Journal of
966 Loss Prevention in the Process Industries 49, 919–928.
967 https://doi.org/10.1016/j.jlp.2017.02.006

968 Turkevich, L.A., Fernback, J., Dastidar, A.G., Osterberg, P., 2016. Potential explosion hazard
969 of carbonaceous nanoparticles: screening of allotropes. Combustion and Flame 167,
970 218–227. https://doi.org/10.1016/j.combustflame.2016.02.010

971 van der Wel, P.G.J., 1993. Ignition and propagation of dust explosions (PhD Thesis). Delft
972 University, The Netherlands.

973 van der Wel, P.G.J., van Veen, J.P.W., Lemkowitz, S.M., Scarlett, B., van Wingerden, C.J.M.,
974 1992. An interpretation of dust explosion phenomena on the basis of time scales.
975 Powder Technology 71, 207–215. https://doi.org/10.1016/0032-5910(92)80010-T

976 Varea, E., 2013. Experimental analysis of laminar spherically expanding flames (thesis).
977 Rouen, INSA.

978 Vignes, A., 2008. Évaluation de l'inflammabilité et de l'explosivité des nanopoudres : une
979 démarche essentielle pour la maîtrise des risques (PhD Thesis). Institut National
980 Polytechnique de Lorraine, France.

981 Vignes, A., Krietsch, A., Dufaud, O., Santandréa, A., Perrin, L., Bouillard, J., 2019. Course of
982 explosion behaviour of metallic powders – From micron to nanosize. Journal of
983 Hazardous Materials 379, 120767. https://doi.org/10.1016/j.jhazmat.2019.120767

984 Wu, H.C., Wu, C.W., Ko, Y.H., 2014. Flame phenomena in nanogrinding process for titanium
985 and iron. J. Loss Prev. Process Ind. 27, 114–118.

986 Zhen, G., Leuckel, W., 1997. Effects of ignitors and turbulence on dust explosions. Journal of
987 Loss Prevention in the Process Industries 10, 317–324. https://doi.org/10.1016/S0950-
988 4230(97)00021-1

989